Nature Geoscience
2022, Volume 15, Pages 293-299
https://doi.org/10.1038/s41561-022-00910-9
https://archimer.ifremer.fr/doc/00759/87127/

Millennial and centennial CO2 release from the Southern Ocean during the last deglaciation

Yu Jimin [1, 2, *], Oppo Delia W. [3], Jin Zhangdong [4], Lacerra Matthew [5], Ji Xuan [2], Umling Natalie E. [6], Lund David C. [7], McCave Nick [8], Menviel Laurie [9], Shao Jun [10], Xu Chen [2]

[1] Pilot National Laboratory for Marine Science and Technology (Qingdao), Qingdao, China
[2] Research School of Earth Sciences, The Australian National University, Canberra, Australian Capital Terriroty, Australia
[3] Department of Geology and Geophysics, Woods Hole Oceanographic Institution, Woods Hole, MA, USA
[4] SKLLQG, Institute of Earth Environment, Chinese Academy of Sciences, Xi'an, China
[5] Department of Geosciences, Princeton University, Princeton, NJ, USA
[6] Department of Earth and Planetary Sciences, American Museum of Natural History, New York, NY, USA
[7] Department of Marine Sciences, University of Connecticut, Groton, CT, USA
[8] Department of Earth Sciences, University of Cambridge, Cambridge, UK
[9] Climate Change Research Centre, Earth and Sustainability Science Research Centre, University of New South Wales, Sydney, New South Wales, Australia
[10] Department of Earth Science, University of Southern California, Los Angeles, CA, USA

Abstract :

For its greenhouse effects, atmospheric CO2 can critically influence the global climate on millennial and centennial timescales. Pleistocene atmospheric CO2 variations must involve changes in ocean storage of carbon, but the mechanisms and pathways of carbon transfer between the oceanic and atmospheric reservoirs are poorly understood due, in part, to complications associated with interpretation of carbonate system proxy data. Here we employ a recently developed approach to reconstruct upper Atlantic air–sea CO2 exchange signatures through the last deglaciation. Using this approach, proxy and model data each suggest that there was a net release of CO2 via the Atlantic sector of the Southern Ocean during the early deglaciation, which probably contributed to the millennial-scale atmospheric CO2 rise during Heinrich Stadial 1 at ~18.0–14.7 kyr ago. Moreover, our data reveal a previously unrecognized mechanism for the centennial-scale atmospheric CO2 rise at the onset of the Bølling warming event around 14.7 kyr ago, namely, the expansion of Antarctic Intermediate Water, a water mass that is especially inefficient at sequestering atmospheric CO2. Our findings highlight the role of the Southern Ocean outgassing and intermediate water-mass production and volume variations in governing millennial- and centennial-timescale atmospheric CO2 rises during the last deglaciation.

Keywords : Biogeochemistry, Ocean sciences, Palaeoceanography, Palaeoclimate

Antarctic ice core data[1] reveal millennial- and centennial-timescale atmospheric CO_2 rises during the last deglaciation between 18 and 10 thousand years ago (ka). Atmospheric CO_2 increased by ~50 ppm during Heinrich Stadial 1 (HS1; ~18-14.7 ka). This millennial increase is generally thought to be linked to Southern Ocean processes including enhanced upwelling, reduced nutrient utilization, and sea ice retreat that assisted the release of ocean carbon to the atmosphere[2-6]. However, evidence is lacking to connect the inferred outgassing at the Southern Ocean surface with the ultimate CO_2 loss from the ocean interior. The origin of centennial atmospheric CO_2 rises is even less clear[7]. For example, the ~12 ppm atmospheric CO_2 rise that occurred within ~200 years at the Bølling onset (~14.7 ka)[8] has been linked to the reinvigoration of North Atlantic Deep Water (NADW)[9-11]. By contrast, other studies suggest processes in the Southern Ocean and North Pacific might have

51 controlled this abrupt CO_2 rise[6,12,13]. To fully understand past carbon cycling, further information from
52 both marine sediments and models is required.

53

54 **Air-sea CO_2 exchange tracers: DIC_{as} and $[CO_3^{2-}]_{as}$**

55 Because air-sea CO_2 exchange directly affects atmospheric CO_2 levels, reconstructing its
56 history can provide critical insights into mechanisms controlling past atmospheric CO_2 variations.
57 While affecting atmospheric CO_2, air-sea CO_2 exchange simultaneously modifies seawater carbonate
58 chemistry. For a closed system without communication with the atmosphere and sediments, seawater
59 dissolved inorganic carbon (DIC) and phosphate ($[PO_4^{3-}]$) would vary following the stoichiometry of
60 biogenic matter (including both soft tissue and hard-part skeletons). As $[PO_4^{3-}]$ is not affected by
61 air-sea gas exchange, a net air-sea CO_2 transfer would decouple the DIC-$[PO_4^{3-}]$ relationship. Thus, a
62 combination of DIC, $[PO_4^{3-}]$ and biogenic matter stoichiometry provides a means to calculate air-sea
63 CO_2 exchange signatures, as originally developed by Broecker and Peng[14]. Built upon ref. [14], Fig. 1
64 shows an air-sea exchange tracer, DIC_{as} (where subscript "as" denotes air-sea exchange), for the
65 preindustrial Atlantic[15,16]. NADW had high DIC_{as} values and acted as a major sink for atmospheric
66 CO_2, because its source waters absorbed atmospheric CO_2 in the North Atlantic, much like today[16-18].
67 By contrast, Antarctic Intermediate Water (AAIW) had the lowest DIC_{as} and was the water mass least
68 efficient at sequestering atmospheric CO_2, reflecting CO_2 outgassing in the Southern Ocean[19]. In the
69 preindustrial Southern Ocean, DIC-rich Circumpolar Deep Waters were upwelled to the surface by
70 prevailing southern westerlies in the Antarctic Zone[2,20,21]. Owing to inefficient biological utilization of
71 nutrients and carbon, the upwelled waters had higher CO_2 partial pressures than the atmosphere,

resulting in CO_2 outgassing[17]. As long as positive sea-to-air CO_2 partially pressure gradients were maintained, upwelled waters continued to outgas CO_2 until they subducted to form AAIW and lost contact with the atmosphere north of the Antarctic Polar Front[17,19,20]. DIC_{as} signals of AAIW would integrate air-sea CO_2 exchange histories in broad areas (both meridionally and zonally) in the Southern Ocean. Due to net CO_2 outgassing in these areas, preindustrial AAIW had low source-water ("preformed") DIC_{as} values (Fig. 1a). Compared to zones at lower latitudes in the Southern Ocean, the Antarctic Zone hosted upwelling regions and had more elevated nutrient and DIC levels, presenting as a stronger CO_2 source to the atmosphere[17,19,20]. Thus, a DIC_{as} decline within AAIW would reflect enhanced CO_2 outgassing, at least, in the Antarctic Zone.

Since no proxy exists for DIC, seawater carbonate ion ($[CO_3^{2-}]$) can be used instead for the geological past. Following ref. [16], tracer $[CO_3^{2-}]_{as}$ can be used to reflect DIC_{as} changes. As can be seen from Fig. 1, $[CO_3^{2-}]_{as}$ shows a strong negative correlation with DIC_{as} (Extended Data Fig. 1). Therefore, reconstructing $[CO_3^{2-}]_{as}$ can place constraints on DIC_{as}, which ultimately reflects air-sea CO_2 exchange. More information about DIC_{as} and $[CO_3^{2-}]_{as}$ is given in the Methods. Simply put, when a water mass sequesters more atmospheric CO_2, it has lower $[CO_3^{2-}]_{as}$ and higher DIC_{as}, and *vice versa*.

If a net amount of CO_2 was outgassed from the Southern Ocean, then a decrease in DIC_{as} and an increase in $[CO_3^{2-}]_{as}$ would be expected in AAIW and its downstream waters. Here, we use cores from the upper Atlantic to investigate air-sea CO_2 exchange histories in the Atlantic sector of the Southern Ocean during the last deglaciation (Figs. 2-4). GGC90 (27.4°S, 46.6°W, 1105 m) from the Brazil

Margin is chosen for its proximity to AAIW and high sedimentation rate during the early deglaciation (Figs. 1,2). Intermediate-water [CO_3^{2-}] and [PO_4^{3-}] reconstructions at GGC90 are from refs. [22,23] (Fig. 4), but these data have not yet been used to infer air-sea CO_2 exchange histories. Importantly, building upon previous work[24], the GGC90 age model is substantially improved by 23 new radiocarbon dates (Fig. 2). To constrain the pathway of air-sea CO_2 exchange, we use NEAP 4K (61.5°N, 24°W, 1627 m) on Bjorn Drift south of Iceland to reconstruct the North Atlantic changes (Figs. 1,3). Benthic $\delta^{13}C$ in NEAP 4K shows the characteristic mid-depth North Atlantic minimum during HS1 (Fig. 3)[25-27], suggesting that this core sufficiently captures major millennial-scale deglacial climatic signals of the region. We present new deep-water [CO_3^{2-}] and [PO_4^{3-}] reconstructions at NEAP 4K using benthic foraminiferal B/Ca and Cd/Ca, respectively (Fig. 3). The NEAP 4K age model is based on 4 new and 13 published[28] radiocarbon dates and new *Neogloboquadrina pachyderma* (sinistral) coiling ratios (Fig. 3). Seawater $[CO_3^{2-}]_{as}$ is calculated following the approach in ref. [16], with a 2σ uncertainty of ~15 μmol/kg. Fig. 5c presents the first continuous $[CO_3^{2-}]_{as}$ records with robust age controls for the Atlantic Ocean during the last deglaciation. DIC_{as} is estimated from $[CO_3^{2-}]_{as}$ using a sensitivity of -0.48 (Extended Data Fig. 2)[16]. Consideration of influences from past changes in biogenic composition and global alkalinity does not affect our conclusion (Extended Data Fig. 3). We also employ an Earth System model[29] to investigate DIC_{as} changes and associated carbon cycling during HS1. See Methods for analytical and calculation details.

DIC_{as} constraint on millennial atmospheric CO_2 changes

Compared to the early Holocene (~10-11.5 ka), intermediate-water [CO_3^{2-}] and [PO_4^{3-}] at GGC90 were lower during the Last Glacial Maximum (LGM; ~18-22 ka) (Fig. 4). These changes deviate from the biological effects which would cause an inverse relationship between seawater [CO_3^{2-}] and [PO_4^{3-}] in a closed system[16]. This suggests that a change in air-sea CO_2 exchange, which must have occurred when waters were in contact with the atmosphere, disrupted the [CO_3^{2-}]-[PO_4^{3-}] relationship in the intermediate South Atlantic. Our calculation shows that compared to the Holocene, LGM intermediate-water [CO_3^{2-}]$_{as}$ at GGC90 was lower by ~30 μmol/kg, corresponding to a ~60 μmol/kg increase in DIC_{as} (Fig. 5c). In the North Atlantic, deep-water [CO_3^{2-}] at NEAP 4K show an LGM-to-Holocene decrease, but this decrease is smaller than the magnitude expected from [PO_4^{3-}] and biogenic matter stoichiometry (Fig. 4; Methods). We calculate that LGM [CO_3^{2-}]$_{as}$ was ~15 μmol/kg lower than the Holocene value, corresponding to a LGM DIC_{as} increase of ~30 μmol/kg at NEAP 4K (Fig. 5c). Together, DIC_{as} increases at GGC90 and NEAP 4K suggest enhanced atmospheric CO_2 storage in the glacial upper Atlantic, lending strong support for more efficient carbon sequestration by both the Southern Ocean and the North Atlantic during the LGM[2-6,16].

During HS1, intermediate-water [CO_3^{2-}] at GGC90 increased but [PO_4^{3-}] remained roughly stable (Fig. 4)[22,23]. These changes lead to a [CO_3^{2-}]$_{as}$ increase by ~25 μmol/kg, corresponding to a DIC_{as} decline by ~50 μmol/kg (Fig. 5c). At NEAP 4K, deep-water [CO_3^{2-}] decreased during HS1 (Fig. 4). Because seawater [CO_3^{2-}] and DIC are generally inversely correlated[30], this [CO_3^{2-}] decrease suggests a DIC increase (~30 μmol/kg) in the mid-depth North Atlantic. Instead of reflecting greater sequestration of atmospheric CO_2, the concomitant [PO_4^{3-}] increase indicates that this DIC increase was largely caused by accumulation of respired carbon due to weakened overturning

circulation[11,27,29,31-33] (Fig. 5b). Our calculation shows little $[CO_3^{2-}]_{as}$ and DIC_{as} change at NEAP 4K during HS1. Unlike $[CO_3^{2-}]$ and $[PO_4^{3-}]$, DIC_{as} in the ocean interior is conservative and can be used to infer DIC_{as} values of source waters (Methods). Neodymium isotope data from the Brazil Margin[34,35] suggest no increase in the mixing proportion of AAIW in the intermediate South Atlantic from the LGM to HS1 (Fig. 5d). Given the roughly stable DIC_{as} at NEAP 4K, the observed DIC_{as} decrease at GGC90 likely reflects (or passively records) a decline in preformed DIC_{as} for AAIW, and hence a net loss of oceanic CO_2 to the atmosphere via the Atlantic sector of the Southern Ocean during HS1. This conclusion can be drawn without using $[CO_3^{2-}]_{as}$ and DIC_{as} tracers, but using them can substantially facilitate interpretation (Methods).

Our inference for HS1 is corroborated by a transient simulation performed with an Earth System model[29] (Fig. 6; Methods). When forced by stronger southern hemisphere westerlies, simulated DIC_{as} decreases in the intermediate South Atlantic (GGC90) and remains roughly stable in the mid-depth polar North Atlantic (NEAP 4K), similar to our proxy reconstructions. Because DIC_{as} increases in the upper ~1 km of the polar North Atlantic (Fig. 6), the DIC_{as} decrease at GGC90 must point to enhanced CO_2 outgassing in the Atlantic sector (and possibly Indo-Pacific sectors) of the Southern Ocean, which is directly supported by simulated air-sea CO_2 fluxes[29]. The enhanced CO_2 outgassing is, at least in part, caused by reduced biological pump efficiency in the Southern Ocean. During HS1, both model and proxy data show nearly constant $[PO_4^{3-}]$ at GGC90[23] (Figs. 4, 6d). Given a possible decrease in respired $[PO_4^{3-}]$ due to enhanced southern ventilation and reduced surface export in the Sub-Antarctic Zone[3,22], the lack of any decline in $[PO_4^{3-}]$ at GGC90 likely indicates a compensating preformed $[PO_4^{3-}]$ increase and hence a weaker biological pump in Antarctic and Polar

157 Front zones during HS1, as supported by model results (Fig. 6d). Moreover, model results show that
158 the distribution of DIC_{as} differs markedly from those of non-conservative tracers including [CO_3^{2-}] and
159 DIC (Fig. 6), highlighting potential pitfalls of relying solely on [CO_3^{2-}] or DIC to infer the ocean's role
160 in affecting atmospheric CO_2. For example, the deep-water DIC increase at NEAP 4K during HS1
161 cannot be interpreted to reflect greater atmospheric CO_2 sequestration at this site due to marginal DIC_{as}
162 variations, but instead indicates enhanced biological respiration (Fig. 6).

163

164 Published surface-water proxies including $\delta^{15}N$ and opal flux suggest generally reduced
165 nutrient utilization and enhanced upwelling in the Antarctic Zone during HS1 (Figs. 5f, g)[2,4,6].
166 However, $\delta^{15}N$ and opal flux mainly reflect surface nutrient utilization during phytoplankton blooming
167 seasons (usually spring/summer), whereas opal flux values and patterns differ spatially in the Antarctic
168 Zone (Extended Data Fig. 4)[2,4,6]. While acknowledging the usefulness of various surface proxies, it
169 remains uncertain whether CO_2 released during one season (or at one location) was absorbed back into
170 the ocean in other seasons (or at another location) before surface waters sank to form
171 intermediate/deep waters. This is exemplified by heterogeneous surface-water CO_2 partial pressures
172 during the preindustrial and last deglaciation in different sectors of the Southern Ocean (Extended
173 Data Fig. 5)[15,36,37]. In contrast to surface-water conditions, AAIW composition changes would
174 integrate effects of air-sea CO_2 exchange during all seasons across broad regions of the Southern
175 Ocean. With NEAP 4K to constrain North Atlantic changes, our reconstructed DIC_{as} decrease in
176 AAIW (GGC90) must require a net CO_2 release via the Atlantic sector of the Southern Ocean during
177 HS1 (Fig. 5c). More specifically, the little change in deep-sea coral $\delta^{15}N$ data (Fig. 5f)[6] has been used
178 to suggest a minor role of the Antarctic Zone in controlling atmospheric CO_2 rise during the early HS1

179 (~18-16.3 ka). By contrast, the large DIC_{as} decline at GGC90, obtained from both proxy and model
180 data (Figs. 5,6), indicates that the Antarctic Zone likely acted as a CO_2 source to the atmosphere during
181 this time. Overall, our data provide strong proxy evidence to bridge a critical gap between enhanced
182 upwelling in the Southern Ocean[2,4,6] and accomplished reduction of atmospheric CO_2 storage in the
183 ocean interior during HS1.

184

185 During the Bølling/Allerød (~14.6-12.9 ka), GGC90 and NEAP 4K data show relatively small
186 variations in $[CO_3^{2-}]$ and $[PO_4^{3-}]$ and hence $[CO_3^{2-}]_{as}$ values (Figs. 4,5c). This implies a roughly stable
187 atmospheric CO_2 storage in the upper Atlantic, a situation favourable for maintaining steady
188 atmospheric CO_2 levels[1] (Fig. 5h). During the Younger Dryas (YD; ~12.9-11.6 ka), deep-water $[CO_3^{2-}]$
189 changed little but $[PO_4^{3-}]$ increased at NEAP 4K, suggesting an ~10 μmol/kg increase in $[CO_3^{2-}]_{as}$ and
190 an ~20 μmol/kg decrease in DIC_{as} (Figs. 4,5c). These signals could be caused by a DIC_{as} decrease
191 associated with AAIW, as expected from enhanced upwelling and reduced nutrient utilization in the
192 Southern Ocean[2,6] (Figs. 5f,g). Unfortunately, the sedimentation at GGC90 is too low (~3 cm/ka; Fig.
193 2) to resolve detailed changes within the YD, warranting future studies to investigate carbon cycling
194 during this time interval.

195

196 **New mechanism for centennial-scale atmospheric CO_2 rise**

197 In addition to millennial-scale changes, data from ~14.5-14.85 ka (corresponding to 72-80 cm)
198 in core GGC90 reveal a centennial-scale intermediate-water $[PO_4^{3-}]$ rise and minimal change in
199 $[CO_3^{2-}]$ (Fig. 4). These data suggest a $[CO_3^{2-}]_{as}$ increase by ~15 μmol/kg, corresponding to a ~30

μmol/kg decrease in DIC_{as} (Fig. 5c). Radiocarbon dates suggest a high sedimentation rate of ~23 cm/ka (~40 year/cm) at this depth range in the core (Fig. 2). Thus, this DIC_{as} decrease occurred within ~350 years or even shorter if taking bioturbation into account. The mid-point (76 cm) of the sediments has an age of 14.7 ± 0.3 ka (1σ), within the age uncertainty of the Bølling onset at 14.7 ± 0.2 ka[8,38]. So, we link the timing of this DIC_{as} decrease to the Bølling onset (Extended Data Fig. 6). At this time, deep-water DIC_{as} at NEAP 4K, a site located much closer to northern-sourced waters, shows little variation (Fig. 5c), pointing to Southern Ocean changes as responsible for the DIC_{as} decrease at GGC90.

The Bølling onset DIC_{as} decrease observed at GGC90 is attributable to two factors: increased Southern Ocean outgassing and AAIW expansion. High-resolution $\delta^{15}N$ and $\delta^{11}B$ data[6,12] measured on deep-sea corals from the Drake Passage indicate enhanced upwelling and a weakened biological pump in the Antarctic Zone at ~14.7 ka (Fig. 5f), which would lower AAIW's preformed DIC_{as} and hence DIC_{as} at GGC90. Northward AAIW expansion at the Bølling onset is supported by increasing εNd at GGC90 (27.4°S) and sites on Demerara Rise (~8°N), nutrient reconstructions for the intermediate North Atlantic (~24°N), and model results (Figs. 5d,e; Extended Data Figs. 7-9)[39-43]. The broad latitudinal range of these data suggest extensive impacts from AAIW expansion at the Bølling onset. We note that GGC90 is located below the core of AAIW (Fig. 1)[42,44]. Because AAIW has low DIC_{as}, a sudden northward expansion of AAIW would decrease intermediate-water DIC_{as} at GGC90 at the Bølling onset (Figs. 1,5; Extended Data Figs. 8).

The abrupt atmospheric CO_2 rise at the Bølling onset has been linked to rapid reinvigoration of NADW[9-11,31], but the exact mechanism linking the two remains elusive. NADW is an efficient water mass to sequester atmospheric CO_2 (Fig. 1). Everything else being equal, its expansion would lower, not raise, atmospheric CO_2. Thus, concomitant processes are required to counteract the effect of NADW expansion. Enhanced Southern Ocean CO_2 outgassing has been suggested for the Bølling onset[6,12]. Based on our data, we propose a new mechanism, namely, AAIW expansion leading to rapid atmospheric CO_2 increase, although our proposal is not mutually exclusive with other hypotheses[9,12,13]. Proxy and model data[33,39-43] suggest that NADW production increased abruptly at ~14.7 ka, necessitating increased northward transport of its source waters including AAIW (Fig. 5a-e; Extended Data Figs. 7-10). Compared to NADW, AAIW had lower DIC_{as} and was less efficient at sequestering atmospheric CO_2 during the last deglaciation, as expected from its higher preformed [PO_4^{3-}] and hence a weaker biological pump[4,6] (Figs. 1,4,5). By reducing air-sea CO_2 storage in the upper Atlantic as manifested by our reconstructed DIC_{as} decline at GGC90, AAIW expansion likely contributed to the ~12 ppm atmospheric CO_2 rise at the Bølling onset (Fig. 5; Extended Data Fig. 6). Due to its modest volume, relatively short residence time, and thus responsiveness to change[21,43], AAIW volume variations present as an attractive candidate to explain abrupt atmospheric CO_2 changes.

In addition to the upper Atlantic, AAIW changes could have a far-reaching impact on the atmospheric CO_2 storage in broader oceanic volumes through altering NADW's compositions. As illustrated in the preindustrial ocean (Fig. 1; Extended Data Fig. 10), northward AAIW transport could lower DIC_{as} of intermediate waters in the (sub-)polar North Atlantic. At least part of these waters would be entrained to form NADW[21,40-42,45], reducing its efficiency to sequester atmospheric CO_2 in

the vast ocean interior that NADW ventilates. Thus, AAIW expansion would decrease DIC_{as} of NADW and thereby counteract any atmospheric CO_2 decline due to NADW reinvigoration and associated volume expansion. A simple calculation shows that AAIW changes could lead to ~4-8 ppm atmospheric CO_2 rise at the Bølling onset (Methods). Despite potentially large uncertainties, our calculation suggests that AAIW changes likely played an important role in the atmospheric CO_2 rise at this time. Nevertheless, the role of AAIW in controlling past atmospheric CO_2 has been underappreciated. Our results highlight the importance of AAIW dynamics in regulating sharp atmospheric CO_2 changes, with profound implications for understanding past and future carbon cycle and climate changes.

Acknowledgments. We thank LX Wu for valuable discussions about AAIW, SF Gu for providing model outputs shown in Fig. 5, EJ Rohling for assisting statistics, and three reviewers for their constructive comments that improved our work. This study is supported by NSFC 42076056 (J.Y.) NSFC41991322 (Z.J.), ARC Discovery Projects DP190100894 (J.Y.), and ARC Future Fellowship FT140100993 (J.Y.) and FT180100606 (L.M.).

Author contributions. J.Y. designed the project and wrote the manuscript. D.W.O. provided critical core materials for new ^{14}C dating and discussed Cd/Ca timing. Z.J. accomplished ^{14}C dating, counted Nps abundance for NEAP 4K, and picked shells for trace element analyses. M.L. contributed to age model discussion. X.J. assisted trace element analyses, uncertainty calculations, and figure preparation. N.E.U./D.C.L. shared published data for GGC90 and discussed age model. N.M. provided NEAP sediments. L.M./J.S. assisted model data. J.S. performed Rampfit analyses. C.X. assisted literature data compilation and figure preparation. All commented on the manuscript.

Competing interests. The authors declare no competing interests.

Correspondence and request for materials should be addressed to J.Y. (jimin.yu@anu.edu.au)

Figure captions:

Fig. 1 | Preindustrial Atlantic air-sea CO_2 exchange tracers. a,**b**, Air-sea CO_2 exchange signatures of dissolved inorganic carbon, DIC_{as} (**a**), and carbonate ion, $[CO_3^{2-}]_{as}$ (**b**). Note that AAIW had most negative DIC_{as} values, presenting the least efficient water mass at sequestering atmospheric CO_2. Also shown in **a** are approximate positions of oceanographic fronts and zones[45]. In **b**, circles represent studied sediment cores, while the inset shows GLODAP hydrographic data used to generate the transects[15,46], following the method described in ref. [16]. NADW = North Atlantic Deep Water, AABW = Antarctic Bottom Water, AAIW = Antarctic Intermediate Water, AZ = Antarctic Zone, PFZ = Polar Front Zone, APF = Antarctic Polar Front, and SAF = Sub-Antarctic Front.

Fig. 2 | Age model for core GGC90. a, Calendar ages against depth. Orange circles and dark green squares are based on planktonic and benthic radiocarbon dates, respectively[24; this study]. Open symbols represent age reversals and are not used for the age model construction. The envelope shows 1σ age uncertainties. The sedimentation rate is ~23 cm/ka before ~14.3 ka, but decreases to ~3 cm/ka afterwards. **b**, Benthic $\delta^{18}O$ (dark green squares) and the LR04 curve (grey curve)[23,47]. Despite age reversals associated with planktonic dates (see Methods and ref. [24] for detailed discussions), benthic $\delta^{18}O$ and ^{14}C data suggest that benthic foraminiferal shells can be used for reliable reconstructions.

Fig. 3 | NEAP 4K deep-water reconstructions and age model. a, *N. pachyderma* (sinistral) coiling ratio (Nps%; blue squares) plotted against NGRIP $\delta^{18}O$[48] (dark grey curve). The age is based on Nps% (triangles) and ^{14}C (crosses) dating methods. **b**, *Cibicidoides wuellerstorfi* B/Ca and reconstructed $[CO_3^{2-}]$[49]. **c**, *C. wuellerstorfi* Cd/Ca and reconstructed seawater Cd and $[PO_4^{3-}]$. The two green circles are based on *Hoeglundina elegans* Cd/Ca. **d**, *C. wuellerstorfi* $\delta^{13}C$[27]. **e**, OxCal simulation results. The envelope shows 1σ age uncertainties. During the last deglaciation, the average sedimentation rate is ~6 cm/ka. HOL = Holocene, YD = Younger Dryas, B/A = Bølling/Allerød, HS1 = Heinrich Stadial 1, and LGM = Last Glacial Maximum.

Fig. 4 | Downcore deep-water chemistry reconstructions. a, carbonate ion content, $[CO_3^{2-}]$. **b**, phosphate content, $[PO_4^{3-}]$. Data for GGC90 and NEAP 4K are from refs [22,23] and this study, respectively. Crosses at the bottom indicate age control points. Bold curves and envelopes show probability maxima and 2σ errors, respectively. Dashed curves indicate expected $[CO_3^{2-}]$ changes relative to 18.5 ka, assuming that biological respiration caused the temporal $[PO_4^{3-}]$ and $[CO_3^{2-}]$ changes without air-sea CO_2 exchange (Methods). GGC90 and NEAP 4K data are coded by red and blue, respectively.

Fig. 5 | Air-sea exchange tracers compared with other records. a, Greenland NGRIP ice-core $\delta^{18}O$[38]. **b**, GGC5 (34°N, 58°W, 4550 m) sedimentary Pa/Th, a proxy for NADW production rates[33]. **c**,

$[CO_3^{2-}]_{as}$ and corresponding DIC_{as} anomalies (ΔDIC_{as}) relative to 18.5 ka for GGC90 (red) and NEAP 4K (blue) with probability maxima (bold curves) and 2σ errors (envelopes). Crosses at the bottom shows age controls. **d**, εNd at GGC90 (red) and at ~670-1100 m (dark yellow) at the Demerara Rise (~8°N)[35,50]. **e**, Modelled cross equator AAIW transport (orange)[43]. **f**, Antarctic Zone (AZ) $\delta^{15}N$ based on deep-sea corals (curve; shading: 2σ) and diatoms (squares)[4,6]. Deep-sea coral $\delta^{15}N$ data are shifted by -7‰ to facilitate plotting with diatom data. **g**, AZ opal flux[2]. **h**, Antarctic ice-core CO_2[1]. Literature records are plotted against their originally published age scales.

Fig. 6 | Model results. a, Anomalies (Δ) in DIC_{as}. **b**, $\Delta[CO_3^{2-}]$. **c**, ΔDIC. **d**, $\Delta[PO_4^{3-}]$. All anomalies indicate changes from 17.4 ka to 16 ka during which Southern Ocean upwelling is enhanced by increasing southern hemisphere westerlies[29]. Circles show locations of sediment cores studied here. See Methods for details.

References:

1 Marcott, S. A. *et al.* Centennial-scale changes in the global carbon cycle during the last deglaciation. *Nature* **514**, 616-619, doi:Doi 10.1038/Nature13799 (2014).

2 Anderson, R. F. *et al.* Wind-driven upwelling in the Southern Ocean and the deglacial rise in atmospheric CO_2. *Science* **323**, 1443-1448 (2009).

3 Martinez-Garcia, A. *et al.* Iron Fertilization of the Subantarctic Ocean During the Last Ice Age. *Science* **343**, 1347-1350, doi:DOI 10.1126/science.1246848 (2014).

4 Studer, A. S. *et al.* Antarctic Zone nutrient conditions during the last two glacial cycles. *Paleoceanogr.* **30**, 845-862, doi:10.1002/2014pa002745 (2015).

5 Stephens, B. B. & Keeling, R. F. The influence of Antarctic sea ice on glacial-interglacial CO2 variations. *Nature* **404**, 171-174, doi:Doi 10.1038/35004556 (2000).

6 Li, T. *et al.* Rapid shifts in circulation and biogeochemistry of the Southern Ocean during deglacial carbon cycle events. *Sci Adv* **6**, eabb3807, doi:10.1126/sciadv.abb3807 (2020).

7 Bauska, T. K. *et al.* Carbon isotopes characterize rapid changes in atmospheric carbon dioxide during the last deglaciation. *P Natl Acad Sci USA* **113**, 3465-3470, doi:10.1073/pnas.1513868113 (2016).

8 Rasmussen, S. O. *et al.* A stratigraphic framework for abrupt climatic changes during the Last Glacial period based on three synchronized Greenland ice-core records: refining and extending the INTIMATE event stratigraphy. *Quat. Sci. Rev.* **106**, 14-28, doi:10.1016/j.quascirev.2014.09.007 (2014).

9 Galbraith, E. D. *et al.* Carbon dioxide release from the North Pacific abyss during the last deglaciation. *Nature* **449**, 890-893 (2007).

10 Barker, S., Knorr, G., Vautravers, M., Diz, P. & Skinner, L. Extreme deepening of the Atlantic overturning circulation during deglaciation. *Nature Geoscience* **3**, 567-571 (2010).

11 Chen, T. *et al.* Synchronous centennial abrupt events in the ocean and atmosphere during the last deglaciation. *Science* **349**, 1537-1541, doi:10.1126/science.aac6159 (2015).

12 Rae, J. W. B. *et al.* CO2 storage and release in the deep Southern Ocean on millennial to centennial timescales. *Nature* **562**, 569-573, doi:10.1038/s41586-018-0614-0 (2018).
13 Gray, W. R. *et al.* Deglacial upwelling, productivity and CO_2 outgassing in the North Pacific Ocean. *Nature Geoscience* **11**, 340-344, doi:10.1038/s41561-018-0108-6 (2018).
14 Broecker, W. & Peng, T. H. Interhemispheric transport of carbon dioxide by ocean circulation. *Nature* **356**, 587-589 (1992).
15 Key, R. M. *et al.* A global ocean carbon climatology: Results from Global Data Analysis Project (GLODAP). *Glob. Biogeochem. Cycle* **18**, doi: 10.1029/2004GB002247, doi:10.1029/2004GB002247 (2004).
16 Yu, J. *et al.* More efficient North Atlantic carbon pump during the Last Glacial Maximum. *Nat Commun* **10**, ARTN 2170, 2110.1038/s41467-41019-10028-z, doi:ARTN 2170, 10.1038/s41467-019-10028-z (2019).
17 Takahashi, T. *et al.* Global sea-air CO_2 flux based on climatological surface ocean pCO_2, and seasonal biological and temperature effects. *Deep-Sea Res. II* **49**, 1601-1622 (2002).
18 Gloor, M. *et al.* A first estimate of present and preindustrial air-sea CO2 flux patterns based on ocean interior carbon measurements and models. *Geophysical Research Letters* **30**, 10-11-10-14, doi:doi:10.1029/2002GL015594 (2003).
19 Gruber, N. *et al.* Oceanic sources, sinks, and transport of atmospheric CO2. *Glob. Biogeochem. Cycle* **23**, doi:Artn Gb1005, 10.1029/2008gb003349 (2009).
20 Sarmiento, J. L. & Gruber, N. *Ocean Biogeochemical Dynamics*. (Princeton University Press, 2006).
21 Talley, L. D. Closure of the Global Overturning Circulation Through the Indian, Pacific, and Southern Oceans: Schematics and Transports. *Oceanography* **26**, 80-97 (2013).
22 Lacerra, M. *et al.* Less Remineralized Carbon in the Intermediate-Depth South Atlantic During Heinrich Stadial 1. *Paleoceanography and Paleoclimatology* **0**, doi:10.1029/2018pa003537 (2019).
23 Umling, N. E. *et al.* Atlantic Circulation and Ice Sheet Influences on Upper South Atlantic Temperatures During the Last Deglaciation. *Paleoceanography and Paleoclimatology* **0**, doi:10.1029/2019pa003558 (2019).
24 Lund, D. C., Tessin, A. C., Hoffman, J. L. & Schmittner, A. Southwest Atlantic water mass evolution during the last deglaciation. *Paleoceanogr.* **30**, 477-494, doi:10.1002/2014PA002657 (2015).
25 Thornalley, D. J. R., Elderfield, H. & McCave, I. N. Intermediate and deep water paleoceanography of the northern North Atlantic over the past 21,000 years. *Paleoceanogr.* **25**, PA1211, doi:1210.1029/2009PA001833 (2010).
26 Oppo, D. W. & Lehman, S. J. Mid-depth circulation of the subpolar North Atlantic during the last glacial maximum. *Science* **259**, 1148-1152 (1993).
27 Rickaby, R. E. M. & Elderfield, H. Evidence from the high-latitude North Atlantic for variations in Antarctic Intermediate water flow during the last deglaciation. *Geochem. Geophys. Geosyst.* **6**, Q05001, doi:05010.01029/02004GC000858 (2005).
28 Hall, I. R., Bianchi, G. G. & Evans, J. R. Centennial to millennial scale Holocene climate-deep water linkage in the North Atlantic. *Quat. Sci. Rev.* **23**, 1529-1536, doi:10.1016/j.quascirev.2004.04.004 (2004).

29 Menviel, L. *et al.* Southern Hemisphere westerlies as a driver of the early deglacial atmospheric CO2 rise. *Nat Commun* **9**, doi:ARTN 2503, 10.1038/s41467-018-04876-4 (2018).
30 Yu, J. *et al.* Sequestration of carbon in the deep Atlantic during the last glaciation. *Nature Geoscience* **9**, 319-324, doi:10.1038/NGEO2657 (2016).
31 Lacerra, M., Lund, D., Yu, J. & Schmittner, A. Carbon storage in the mid-depth Atlantic during millennial-scale climate events. *Paleoceanogr.* **32**, 780-795, doi:10.1002/2016PA003081 (2017).
32 Schmittner, A. & Lund, D. C. Early deglacial Atlantic overturning decline and its role in atmospheric CO2 rise inferred from carbon isotopes (delta C-13). *Climate of the Past* **11**, 135-152, doi:10.5194/cp-11-135-2015 (2015).
33 McManus, J. F., Francois, R., Gherardi, J. M., Keigwin, L. D. & Brown-Leger, S. Collapse and rapid resumption of Atlantic meridional circulation linked to deglacial climate changes. *Nature* **428**, 834-837, doi:Doi 10.1038/Nature02494 (2004).
34 Howe, J. N. W. *et al.* Similar mid-depth Atlantic water mass provenance during the Last Glacial Maximum and Heinrich Stadial 1. *Earth Planet. Sci. Lett.* **490**, 51-61, doi:https://doi.org/10.1016/j.epsl.2018.03.006 (2018).
35 Poppelmeier, F. *et al.* Water mass gradients of the mid-depth Southwest Atlantic during the past 25,000 years. *Earth Planet. Sci. Lett.* **531**, doi:ARTN 115963, 10.1016/j.epsl.2019.115963 (2020).
36 Moy, A. D. *et al.* Varied contribution of the Southern Ocean to deglacial atmospheric CO2 rise. *Nature Geoscience* **12**, 1006-+, doi:10.1038/s41561-019-0473-9 (2019).
37 Martinez-Boti, M. A. *et al.* Boron isotope evidence for oceanic carbon dioxide leakage during the last deglaciation. *Nature* **518**, 219-U154, doi:10.1038/nature14155 (2015).
38 Veres, D. *et al.* The Antarctic ice core chronology (AICC2012): an optimized multi-parameter and multi-site dating approach for the last 120 thousand years. *Climate of the Past* **9**, 1733-1748, doi:10.5194/cp-9-1733-2013 (2013).
39 Liu, Z. *et al.* Transient simulation of last deglaciation with a new mechanism for Bolling-Allerod warming. *Science* **325**, 310-314, doi:DOI 10.1126/science.1171041 (2009).
40 Came, R. E., Oppo, D. W. & Curry, W. B. Atlantic Ocean circulation during the Younger Dryas: Insights from a new Cd/Ca record from the western subtropical South Atlantic. *Paleoceanogr.* **18**, Artn 1086, doi: 1010.1029/2003pa000888, doi:10.1029/2003pa000888 (2003).
41 Came, R. E., Oppo, D. W., Curry, W. B. & Lynch-Stieglitz, J. Deglacial variability in the surface return flow of the Atlantic meridional overturning circulation. *Paleoceanogr.* **23**, Artn Pa1217, doi:10.1029/2007pa001450 (2008).
42 Oppo, D. & Curry, W. Deep Atlantic Circulation During the Last Glacial Maximum and Deglaciation. *Nature Education Knowledge* **3**, 1 (2012).
43 Gu, S. F. *et al.* Coherent Response of Antarctic Intermediate Water and Atlantic Meridional Overturning Circulation During the Last Deglaciation: Reconciling Contrasting Neodymium Isotope Reconstructions From the Tropical Atlantic. *Paleoceanogr.* **32**, 1036-1053, doi:10.1002/2017pa003092 (2017).
44 Curry, W. B. & Oppo, D. Glacial water mass geometry and the distribution of $\delta^{13}C$ of ΣCO_2 in the western Altantic Ocean. *Paleoceanogr.* **20**, PA1017, doi:1010.1029/2004PA001021 (2005).

45 Talley, L. D., Pickard, G. L., Emery, W. J. & Swift, J. H. *Descriptive Physical Oceanography: An Introduction (Sixth Edition)*. (Elsevier, 2011).
46 Schlitzer, R. Ocean Data View. **https://odv.awi.de/** (2006).
47 Lisiecki, L. E. & Raymo, M. E. A Pliocene-Pleistocene stack of 57 globally distributed benthic $\delta^{18}O$ records. *Paleoceanogr.* **20**, PA1003, doi:1010.1029/2004PA001071 (2005).
48 NGRIP_members. High-resolution record of Northern Hemisphere climate extending into the last interglacial period. *Nature* **431**, 147-151, doi:Doi 10.1038/Nature02805 (2004).
49 Yu, J. M. & Elderfield, H. Benthic foraminiferal B/Ca ratios reflect deep water carbonate saturation state. *Earth Planet. Sci. Lett.* **258**, 73-86, doi: 10.1016/j.epsl.2007.1003.1025 (2007).
50 Huang, K. F., Oppo, D. W. & Curry, W. B. Decreased influence of Antarctic intermediate water in the tropical Atlantic during North Atlantic cold events. *Earth Planet. Sci. Lett.* **389**, 200-208, doi:10.1016/j.epsl.2013.12.037 (2014).

Methods

Air-sea CO_2 exchange tracers: DIC_{as} and $[CO_3^{2-}]_{as}$. Various methods have been used to investigate past carbon cycle (e.g., refs [2,51-59]). Here we employ air-sea CO_2 exchange tracers, DIC_{as} and $[CO_3^{2-}]_{as}$, to investigate how the storage of atmospheric CO_2 changed in the ocean interior during the last deglaciation. Due to their novelty and innate applications to paleoceanography, we briefly describe concepts of DIC_{as} and $[CO_3^{2-}]_{as}$. We refer the reader to ref. [16] for calculation details. Assuming no air-sea exchange, $[PO_4^{3-}]$–DIC of a package of water would be coupled and change following the biogenic matter stoichiometry (including Redfield ratio and rain ratio, the latter of which indicates the soft-to-hard part molar carbon ratio)[14]. If a net air-sea CO_2 exchange occurs, then DIC–$[PO_4^{3-}]$ would decouple. The air-sea CO_2 exchange signal can be described using DIC_{as}, following the approach from Broecker and Peng[14]. This approach has been used to calculate anthropogenic CO_2 in the ocean by recent studies (e.g., ref. [60]) as well as glacial air-sea CO_2 exchange histories (ref. [16]; see also Fig. 6). The approach corrects for DIC changes due to evaporation and precipitation effects, and within ocean

462 DIC redistribution associated with organic carbon and $CaCO_3$ production and deconstructions. After
463 these corrections, we can obtain DIC_{as} which reflects the net effect of air-sea CO_2 exchange that occurs
464 at the ocean-atmosphere interface[16]. Fig. 1a shows the DIC_{as} distribution in the preindustrial Atlantic
465 Ocean using the GLODAP data set[15].
466
467 Owing to the lack of a quantitative proxy for DIC, we use a linked CO_2 system parameter,
468 $[CO_3^{2-}]$, to calculate another air-sea CO_2 tracer termed $[CO_3^{2-}]_{as}$ (Fig.1 b), which is used to reflect
469 changes in $[CO_3^{2-}]$ due to air-sea CO_2 exchange[16]. The calculation accounts for effects of temperature,
470 salinity, and pressure changes (because these changes would affect $[CO_3^{2-}]$ via affecting the CO_2
471 system dissociation constants, even without any net air-sea CO_2 exchange), and corrects for
472 within-ocean DIC redistribution associated with biological processes as is done for DIC_{as} calculations.
473 As expected from the CO_2 system theory[30], DIC_{as} and $[CO_3^{2-}]_{as}$ are strongly negatively correlated (Fig.
474 1; Extended Data Fig. 1).
475
476 DIC_{as} and $[CO_3^{2-}]_{as}$ are calculated using a reference condition of $[PO_4^{3-}]$ = 2.2 μmol/kg (the
477 global mean ocean value), salinity = 35‰, temperature = 3°C, and pressure = 2500 dbar. Using a
478 different reference condition (e.g., $[PO_4^{3-}]$ = 1.3 μmol/kg) has no effect on their spatial/temporal
479 patterns or their correlation. See ref. [16] for detailed discussions.
480
481 It is important to note that air-sea CO_2 exchange signals induced by marine biological and
482 physical processes are preserved during the $[CO_3^{2-}]_{as}$ calculations. To better understand our
483 calculations, we present the following two examples.

1. Cooling at a certain deep-water formation region would decrease [CO_3^{2-}] for two reasons: (*i*) changes in the CO_2 system dissociation constants due to cooling, and (*ii*) more atmospheric CO_2 absorption due to an enhanced solubility pump. In contrast to (*ii*), no air-sea CO_2 change is involved in (*i*). In the calculation of $[CO_3^{2-}]_{as}$, the temperature correction only removes influences from (*i*) but preserves the effect of air-sea CO_2 exchange from (*ii*).
2. An enhanced nutrient utilization can have the following two effects: (*i*) to decrease surface nutrient and DIC due to phytoplankton consumption, which increases seawater [CO_3^{2-}], and (*ii*) to lower surface CO_2 partial pressure and absorb more atmospheric CO_2, which decreases seawater [CO_3^{2-}]. Only (*ii*) involves air-sea CO_2 exchange. Our $[CO_3^{2-}]_{as}$ calculation only corrects for the effect from (*i*).

Seawater $[CO_3^{2-}]_{as}$ has the following characteristics:

- A water mass' source-water (i.e., "preformed") $[CO_3^{2-}]_{as}$ integrates the effects of processes including solubility (linked to temperature and salinity changes) and biological (linked to nutrient changes) pump strengths, air-sea contact time (affected by surface residence time of source waters and sea ice covers), and gas exchange rates (linked to wind speeds)[17,61,62].
- Preformed $[CO_3^{2-}]_{as}$ reflects the net CO_2 exchange (by all processes mentioned above) between the ocean and the atmosphere at the ocean surface prior to sinking.
- More CO_2 absorption would lead to lower preformed $[CO_3^{2-}]_{as}$, and *vice versa*.
- In the ocean interior, a $[CO_3^{2-}]_{as}$ at any location is determined by preformed $[CO_3^{2-}]_{as}$ values of water masses involved and their mixing proportions.

- During water mass mixing, $[CO_3^{2-}]_{as}$ is conservative, not affected by DIC or $[PO_4^{3-}]$ changes associated with biological respiration.
- Given a knowledge about water mass mixing, $[CO_3^{2-}]_{as}$ changes in the ocean interior can be used to infer preformed $[CO_3^{2-}]_{as}$ changes, which provides information about air-sea exchange at the surface.
- Compared to $[CO_3^{2-}]$ which is affected by biological respiration, using $[CO_3^{2-}]_{as}$ allows more direct links to atmospheric CO_2 changes.
- The ***calculation*** of seawater $[CO_3^{2-}]_{as}$ involves $[CO_3^{2-}]$ and $[PO_4^{3-}]$, but does not require a prior knowledge about preformed $[PO_4^{3-}]$ values. This does ***not*** mean preformed $[PO_4^{3-}]$ changes have no effect on $[CO_3^{2-}]_{as}$, because they often do via changing surface CO_2 partial pressure and air-sea CO_2 flux. For an example, see "Other approaches to interpret GGC90 data during HS1" below.
- A package of water with a higher $[CO_3^{2-}]_{as}$ stores less atmospheric CO_2 (or releases more CO_2 to the atmosphere), and *vice versa*.
- The temporal evolution of seawater $[CO_3^{2-}]_{as}$ may be affected by the global alkalinity and DIC changes associated with $CaCO_3$ input-output imbalances between the ocean and sediments, but the effect is generally gradual[63] and can be investigated based on marine sediment evidence and simulation results (see Extended Data Fig. 3).

Cores, samples, analytical methods, and age models. For GGC90, benthic foraminiferal B/Ca and Cd/Ca data are from Lacerra et al.[22] and Umling et al.[23], respectively. Built upon previous work[24], the age model of the core is improved by 5 new planktonic radiocarbon dates (Fig. 2). While there are clear

age reversals in the planktonic foraminiferal ^{14}C results, stable isotope analyses of individual benthic foraminifera show limited effect of bioturbation in this core. As discussed in Lund et al. (2015)[24], the age reversals reflect downward burrowing of carbonate-rich Holocene age material with abundant planktonic foraminifera but sparse benthic foraminifera. As a result, the planktonic ^{14}C age model can display age reversals while the benthic $\delta^{18}O$ time series lack evidence of bioturbation. The robustness of our age model is corroborated by 18 new benthic foraminiferal radiocarbon dates (Fig. 2). At GGC90, no large surface reservoir age is expected due to its subtropical gyre setting where air-sea radiocarbon exchange is close to equilibrium[23]. Previous work suggests little change in the ventilation ages at intermediate water depths off the Brazil Margin[64]. We thus converted radiocarbon ages converted into calendar ages using the CALIB 7.01[65] with the Marine13 calibration curve[66] and ΔR values of 0±200 years (planktonics) and 1000±200 years (benthics) (1σ). The age uncertainty is estimated using the OxCal program[67]. At GGC90, sedimentation rates varied from ~3 cm/ka during 10-14.3 ka to ~23 cm/ka during 14.3-20 ka (Fig. 2), favourable for early deglacial reconstructions.

For NEAP 4K, about 20 cm^3 of sediment from each sample (~1 cm thickness) was disaggregated in de-ionized water and was wet sieved through 63 μm sieves. The epifaunal benthic foraminiferal species *C. wuellerstorfi* was picked from the 250-500 μm size fraction. To ensure comparability of data with GGC90, we used the same analytical procedures to measure trace elements in NEAP 4K. For each sample, ~10-20 shells were picked and then double checked under a microscope before crushing to ensure that consistent morphologies were used throughout the core. For trace element analyses (n = 28 pairs), all foraminiferal shells were cleaned with the "Cd-cleaning" protocol[27,68,69]. Benthic B/Ca and Cd/Ca ratios (Fig. 3) were measured on an inductively-coupled plasma mass spectrometer

549 (ICP-MS) using procedures outlined in ref. [70], with an analytical error better than ~4% (2σ). Mn/Ca
550 and Al/Ca were also measured, and they showed no correlation with Cd/Ca or B/Ca, suggesting
551 minimal influences from silicate or diagenetic coatings. The age model for NEAP 4K is based on
552 published[28] and new radiocarbon dates as well as new *Neogloboquadrina pachyderma* (sinistral)
553 abundance counting (Fig. 3). Radiocarbon ages were converted into calendar ages using the CALIB
554 7.01[65] with the Marine13 calibration curve[66]. Previous work[71] suggested significant increases in
555 glacial surface reservoir ages at the core location, possibly linked to insufficient air-sea radiocarbon
556 exchange in the polar North Atlantic. Following ref. [72], surface ΔR values are assigned to be 0±200
557 years and 400±500 years (1σ) for <165 cm (corresponding to the Holocene) and >180 cm
558 (corresponding to the LGM), respectively. No radiocarbon dating is used for the HS1. Uncertainties of
559 the age model are estimated using the OxCal program[67]. Our data reveal a mean sedimentation rate of
560 ~6 cm/ka during the last deglaciation (Fig. 3).
561
562 **Benthic B/Ca to deep-water [CO_3^{2-}].** At NEAP 4K, deep-water [CO_3^{2-}] values are reconstructed
563 using benthic B/Ca[30,49] from $[CO_3^{2-}]_{downcore} = [CO_3^{2-}]_{PI} + \Delta B/Ca_{downcore\text{-}coretop}/k$, where $[CO_3^{2-}]_{PI}$ is the
564 preindustrial (PI) deep-water [CO_3^{2-}] value estimated from the GLODAP dataset[15], $\Delta B/Ca_{downcore\text{-}coretop}$
565 represents the deviation of B/Ca of down-core samples from the core-top value, and k is the
566 B/Ca-[CO_3^{2-}] sensitivity of *C. wuellerstorfi* (1.14 μmol/mol per μmol/kg)[49]. We use a reconstruction
567 uncertainty (2σ) of 10 μmol/kg in [CO_3^{2-}] based on global core-top calibration samples[49,73]. For
568 GGC90, deep-water [CO_3^{2-}] reconstructions are reconstructed using *Cibicidoides pachyderma* B/Ca
569 (ref. [22]) and a calibration specific to this species (ref. [74]), with a reconstruction error of 10 μmol/kg
570 (2σ).

571

572 **Benthic Cd/Ca to deep-water [PO_4^{3-}].** For NEAP 4K, we follow the established approach[75-77] to
573 convert *C. wuellerstorfi* Cd/Ca into deep-water Cd concentrations. We use a partition coefficients
574 (D_{Cd}) of 2.2[27] to calculate deep water Cd from: Cd (nmol/kg) = $[(Cd/Ca)_{foram}/D_{Cd}] \times 10$. The abundance
575 of *Hoeglundina elegans* in NEAP 4K is very low, but measurements on a few *H. elegans* samples yield
576 consistent Cd results with those based on *C. wuellerstorfi* (Fig. 3). Benthic Cd/Ca from this core were
577 measured previously[27], but we prefer to use our new Cd/Ca which were measured using the same
578 solutions for B/Ca. This is because paired Cd/Ca and B/Ca measurements based on the same solutions
579 are conducive to improving the accuracy of $[CO_3^{2-}]_{as}$ reconstructions. For GGC90, intermediate water
580 Cd is reconstructed using *H. elegans* Cd/Ca and a D_{Cd} of 1, as published by Umling et al.[23]. Seawater
581 Cd is converted into $[PO_4^{3-}]$ using the relationship from ref. [78]. Using other equations has little impact
582 on the pattern of our reconstructions. Previous studies (e.g., refs [79,80]) employing the same
583 reconstruction approach have used ~6-9% errors (2σ) with $[PO_4^{3-}]$. To be conservative, we assign 10%
584 uncertainty (2σ) for our $[PO_4^{3-}]$ reconstructions.

585

586 **Deep-water temperature, salinity, and pressure estimates.** For NEAP 4K, deep-water temperature
587 (T) is estimated from the ice volume corrected benthic $\delta^{18}O$ ($\delta^{18}O_{IVC}$) and the $\delta^{18}O$-temperature
588 equation of Marchitto et al.[81] from: $T = 2.5 - (\delta^{18}O_{IVC} - 2.8)/0.224$, where $\delta^{18}O_{IVC} = \delta^{18}O_{benthic} -$
589 $\delta^{18}O_{global\_sealevel}$. $\delta^{18}O_{global\_sealevel}$ was estimated from sea level curves[82,83] with a global $\delta^{18}O_{seawater}$–sea
590 level scaling of 0.0085‰/m[84]. For GGC90, T is reconstructed using *H. elegans* Mg/Li[23]. Owing to the
591 relative weak sensitivity of $[CO_3^{2-}]$ to T and narrow deep-water T variations in the past, using other
592 methods to estimate T would negligibly affect our final $[CO_3^{2-}]_{as}$ values. Deep-water salinity (S) is

593 calculated by: $S = S_{core\_top} + 1.11 \times \delta^{18}O_{global\_sealevel}$, where S_{core_top} is the modern S (34.95 and 34.34 at
594 NEAP 4K and GGC90, respectively[15]) and the term 1.11 is the scaling factor for a global
595 $S-\delta^{18}O_{global\_sealevel}$ relationship[20,84]. We assume 1°C and 1‰ uncertainties (2σ) in T and S, respectively.
596 Deep water pressure (P) is estimated using today's water depths (1627 m and 1105 m for NEAP 4K
597 and GGC90, respectively) and past relative sea level (RSL) reconstructions from: P = today's water
598 depth – RSL.
599
600 **$[CO_3^{2-}]_{as}$ and DIC_{as} calculations.** Following the approach in ref. [16], calculation of $[CO_3^{2-}]_{as}$ involves
601 two steps. First, we calculate normalized ($[CO_3^{2-}]_{Norm}$) to account for salinity (S), temperature (T) and
602 pressure (P) effects on $[CO_3^{2-}]$ using the following equation:
603 $$[CO_3^{2-}]_{Norm} = [CO_3^{2-}] + (35 - S) \times Sen_{\_S} + (3 - T) \times Sen_{\_T} + (2500 - P)/100 \times Sen_{\_P} \quad (1)$$
604 where $Sen_{\_S}$, $Sen_{\_T}$, and $Sen_{\_P}$ represent sensitivities to S, T, and P (3 μmol/kg per ‰ change in S, 0.5
605 μmol/kg per °C, and 0.1 μmol/kg per 100 dbar) as defined and shown in Fig. 4 of ref. [16]. Then, $[CO_3^{2-}]_{as}$
606 is calculated by:
607 $$[CO_3^{2-}]_{as} = [CO_3^{2-}]_{Norm} + ([PO_4^{3-}] - 2.2) \times [CO_3^{2-}]_{Norm}/[PO_4^{3-}] \text{ sensitivity} - 78 \quad (2)$$
608 where $[CO_3^{2-}]_{Norm}/[PO_4^{3-}]$ sensitivity is the sensitivity of $[CO_3^{2-}]_{Norm}$ to $[PO_4^{3-}]$ changes due to
609 biological processes (see Fig. 4 in ref. [16] for details), 2.2 represents the global mean ocean $[PO_4^{3-}]$, and
610 78 is an arbitrary term. In Fig. 5, we use sensitivities based on a Redfield ratio ($C/[PO_4^{3-}]$) of 127 and a
611 rain ratio (R) of 4. Using other $C/[PO_4^{3-}]$ and R values[85,86] does not affect our conclusions (Extended
612 Data Fig. 3).
613 The error associated with $[CO_3^{2-}]_{as}$ is calculated using the following equation:

$$2\sigma_{\left[CO_3^{2-}\right]_{as}}=\left[\left(\frac{\partial_{\left[CO_3^{2-}\right]_{as}}}{\partial_{\left[CO_3^{2-}\right]}}\times 2\sigma_{\left[CO_3^{2-}\right]}\right)^2+\left(\frac{\partial_{\left[CO_3^{2-}\right]_{as}}}{\partial_S}\times 2\sigma_S\right)^2+\left(\frac{\partial_{\left[CO_3^{2-}\right]_{as}}}{\partial_{Sen\_S}}\times 2\sigma_{Sen\_S}\right)^2+\left(\frac{\partial_{\left[CO_3^{2-}\right]_{as}}}{\partial_T}\times 2\sigma_T\right)^2+\left(\frac{\partial_{\left[CO_3^{2-}\right]_{as}}}{\partial_{Sen\_T}}\times 2\sigma_{Sen\_T}\right)^2+\left(\frac{\partial_{\left[CO_3^{2-}\right]_{as}}}{\partial_P}\times 2\sigma_P\right)^2+\left(\frac{\partial_{\left[CO_3^{2-}\right]_{as}}}{\partial_{Sen\_P}}\times 2\sigma_{Sen\_P}\right)^2+\left(\frac{\partial_{\left[CO_3^{2-}\right]_{as}}}{\partial_{\left[PO_4^{3-}\right]}}\times 2\sigma_{\left[PO_4^{3-}\right]}\right)^2+\left(\frac{\partial_{\left[CO_3^{2-}\right]_{as}}}{\partial_{\left[CO_3^{2-}\right]_{Norm}/\left[PO_4^{3-}\right]\text{ sensitivity}}}\times 2\sigma_{\left[CO_3^{2-}\right]_{Norm}/\left[PO_4^{3-}\right]\text{ sensitivity}}\right)^2\right]^{\frac{1}{2}}$$

-- (3)

where $\frac{\partial_{\left[co_3^{2-}\right]_{as}}}{\partial_{\left[CO_3^{2-}\right]}}=1$, $\frac{\partial_{\left[co_3^{2-}\right]_{as}}}{\partial_S}=-Sen\_S$, $\frac{\partial_{\left[CO_3^{2-}\right]_{as}}}{\partial_{Sen\_S}}=35-S$, $\frac{\partial_{\left[co_3^{2-}\right]_{as}}}{\partial_T}=-Sen\_T$, $\frac{\partial_{\left[CO_3^{2-}\right]_{as}}}{\partial_{Sen\_T}}=3-T$, $\frac{\partial_{\left[co_3^{2-}\right]_{as}}}{\partial_P}=-Sen\_P/100$, $\frac{\partial_{\left[CO_3^{2-}\right]_{as}}}{\partial_{Sen\_P}}=25-P/100$, $\frac{\partial_{\left[co_3^{2-}\right]_{as}}}{\partial_{PO_4^{3-}}}=[CO_3^{2-}]_{Norm}/[PO_4^{3-}]\text{ sensitivity}$, and $\frac{\partial_{\left[co_3^{2-}\right]_{as}}}{\partial_{[co_3^{2-}]_{Norm}/[PO_4^{3-}]\text{ sensitivity}}}=[PO_4^{3-}]-2.2$. Based on uncertainties with individual parameters used, we obtain an average error in $[CO_3^{2-}]_{as}$ of 15 μmol/kg (2σ).

It is worth noting that $[CO_3^{2-}]_{as}$ calculations for all samples from NEAP 4K and majority of samples from GGC90 are based on paired $[CO_3^{2-}]$ and $[PO_4^{3-}]$ reconstructions using the same solutions (NEAP 4K) or co-existing shells (GGC90). This enables the two key parameters, $[CO_3^{2-}]$ and $[PO_4^{3-}]$, needed for computing $[CO_3^{2-}]_{as}$ to be estimated for the same shell growth environments, conducive to improving the accuracy of $[CO_3^{2-}]_{as}$ reconstructions.

626 DIC_{as} changes (ΔDIC_{as}) are calculated from $[CO_3^{2-}]_{as}$ changes ($\Delta[CO_3^{2-}]_{as}$) using: ΔDIC_{as} =
627 $\Delta[CO_3^{2-}]_{as} \div [CO_3^{2-}]_{as}/DIC_{as}$ sensitivity. At NEAP 4K and GGC90, deglacial $[CO_3^{2-}]_{Norm}$ ranges from
628 ~70 to 100 μmol/kg (here, $[CO_3^{2-}]_{Norm} = [CO_3^{2-}]_{as} + 78$), corresponding to $[CO_3^{2-}]_{as}/DIC_{as}$ sensitivities
629 of -0.43 to -0.53 (Extended Data Fig. 2). We use a mean sensitivity of -0.48 to estimate ΔDIC_{as} shown
630 in Fig. 5c.
631
632 **Statistical analyses.** Here we focus on millennial- and centennial-scale trends defined by multiple
633 data points based on statistical analyses, and refrain from interpreting shorter timescale variations
634 revealed by individual reconstructions. Uncertainties associated with $[CO_3^{2-}]$, $[PO_4^{3-}]$, and $[CO_3^{2-}]_{as}$
635 were evaluated using a Monte-Carlo approach[87,88]. Errors associated with the chronology (x-axis) and
636 $[CO_3^{2-}]$, $[PO_4^{3-}]$, and $[CO_3^{2-}]_{as}$ reconstructions (y-axis) are considered during error propagation. Age
637 errors are estimated using OxCal (see above)[67]. Methods to calculate errors associated with individual
638 $[CO_3^{2-}]$ and $[PO_4^{3-}]$, $[CO_3^{2-}]_{as}$ reconstructions (y-axis) are given above. All data points were sampled
639 separately and randomly 5,000 times within their chronological and $[CO_3^{2-}]$ (or $[PO_4^{3-}]$, $[CO_3^{2-}]_{as}$)
640 uncertainties, and each iteration was then interpolated linearly. At each time step, the probability
641 maximum and data distribution uncertainties of the 5,000 iterations were assessed. Figs. 4 and 5 show
642 probability maxima (bold curves) and ±95% (light grey; 2.5^{th}-97.5^{th} percentile) probability intervals
643 for the data distributions, including chronological and proxy uncertainties. For details, see refs [87,88].
644 To objectively assess timing of ΔDIC_{as} at GGC90 and atmospheric CO_2 changes at ~14.7 ka, we
645 employed the Rampfit software[89]. As can be seen from Extended Data Fig. 6, the ΔDIC_{as} decline was
646 concurrent with the ~12 ppm atmospheric CO_2 rise at the Bølling onset, consistent with Monte-Carlo
647 results (Figs. 5c,h).

Expected [CO_3^{2-}] calculation (Fig. 4). For a package of water that has no exchange of CO_2 with the atmosphere and sediments, its [CO_3^{2-}] and [PO_4^{3-}] can be altered by varying amounts of biological matter respired. In this case, changes in [CO_3^{2-}] and [PO_4^{3-}] vary following the biogenic matter stoichiometry (including Redfield ratio and rain ratio). This provides a means to calculate the expected [CO_3^{2-}] changes for a water mass solely driven by biological recycling of carbon and nutrient within the ocean, if its [PO_4^{3-}] changes are known. For down core calculations, we use [PO_4^{3-}] and [CO_3^{2-}] at 18.5 ka as reference values. The choice of 18.5 ka is to facilitate consideration of changes relative to the LGM, and using values at other ages does not affect our conclusion. For other times, [PO_4^{3-}] changes ($\Delta[PO_4^{3-}]$) relative to 18.5 ka are calculated by: $\Delta[PO_4^{3-}] = [PO_4^{3-}] - [PO_4^{3-}]_{@18.5ka}$. Regarding [$CO_3^{2-}$] calculations, we first convert in-situ [CO_3^{2-}] at 18.5 ka into $[CO_3^{2-}]_{Norm@18.5ka}$ using equation (1). Then, the expected $[CO_3^{2-}]_{Norm}$ values at other ages are calculated by: expected $[CO_3^{2-}]_{Norm} = [CO_3^{2-}]_{Norm@18.5ka} + \Delta[PO_4^{3-}] \times [CO_3^{2-}]_{Norm}/[PO_4^{3-}]$ sensitivity. Afterwards, the expected $[CO_3^{2-}]_{Norm}$ is converted back into expected in-situ [CO_3^{2-}] (dashed curves in Fig. 4a) to account for effects from T-S-P changes through time, a reversion for calculating $[CO_3^{2-}]_{Norm}$. Note that this expected in-situ [CO_3^{2-}] assumes no air-sea CO_2 exchange during the calculation.

Other approaches to interpret GGC90 data during HS1. In the main text, we have used $[CO_3^{2-}]_{as}$ to infer enhanced Southern Ocean CO_2 outgassing during HS1. Here, we demonstrate that the same conclusion can also be reached by combined use of [PO_4^{3-}] and [CO_3^{2-}], without using $[CO_3^{2-}]_{as}$. During HS1, intermediate-water [PO_4^{3-}] remained roughly stable while [CO_3^{2-}] increased at site

669 GGC90. Given little increase in the mixing proportion of AAIW at GGC90[34,35] (Fig. 5d, e), we
670 consider the following scenarios from the LGM to HS1:

671 (i) AAIW's preformed [PO_4^{3-}] stayed stable. This would require no change in respired carbon
672 and higher preformed [CO_3^{2-}]. However, the required little change in respired carbon is
673 inconsistent with reduced export and remineralization in the South Atlantic during the early
674 last deglacial[3,22]. Thus, we consider this possibility unfeasible.

675 (ii) AAIW's preformed [PO_4^{3-}] decreased. This would require greater respired carbon to keep
676 intermediate-water [PO_4^{3-}] at a stable level at GGC90. A lower preformed [PO_4^{3-}] would
677 imply a stronger biological pump, which would limit CO_2 outgassing and thus store more
678 carbon in the ocean, with an effect to lower seawater [CO_3^{2-}][30]. Not only does this scenario
679 contradict the observed reduction in phytoplankton export[3], but greater biological
680 respiration would also lower seawater [CO_3^{2-}] of AAIW, inconsistent with reconstructed
681 [CO_3^{2-}] at GGC90. Thus, we discard this possibility.

682 (iii) AAIW's preformed [PO_4^{3-}] increased. The stable intermediate-water [PO_4^{3-}] at GGC90
683 would require a reduction in respired carbon, consistent with proxy results[22]. Also,
684 increased preformed [PO_4^{3-}] suggests a weaker biological pump in the Southern Ocean,
685 consistent with opal flux and $\delta^{15}N$ data (Fig. 5)[2,4,54]. This further implies enhanced
686 outgassing of CO_2 via the Southern Ocean, contributing to a [CO_3^{2-}] increase in AAIW as
687 manifested by the reconstruction at GGC90. Thus, this scenario is consistent with
688 intermediate-water [PO_4^{3-}] and [CO_3^{2-}] at GGC90 as well as other proxy and model
689 data[2,4,29,54].

690

691 Based on consideration of various scenarios above, intermediate-water [PO_4^{3-}] and [CO_3^{2-}] at
692 GGC90 most likely reflect CO_2 outgassing via the Southern Ocean during HS1. As demonstrated in
693 the main text, it is more straightforward to use $[CO_3^{2-}]_{as}$ to infer air-sea CO_2 exchanges. Due to its
694 conservative nature, $[CO_3^{2-}]_{as}$ can be used to infer preformed value changes, which can then be further
695 used to infer air-sea gas exchange associated with source waters.
696
697 **Model results.** We use results from a transient simulation[29] to explore and corroborate feasibility of
698 our air-sea tracers and associated pathways of the early deglacial CO_2 release from the ocean to the
699 atmosphere. Fig. 6 shows results for the "LH1-SO-SHW" transient simulation of the last deglaciation
700 using the Earth System Model LOVECLIM[29]. Details on the experimental set-up are provided in ref.
701 [29]. Briefly, LOVECLIM includes an ocean general circulation model (3° by 3° and 20 vertical levels)
702 coupled to a dynamic/thermodynamic sea-ice model, a quasi-geostrophic T21 atmospheric model, a
703 land surface and vegetation model, and a terrestrial and marine carbon cycle[90]. The LGM state is
704 obtained by forcing the model with appropriate boundary conditions (i.e., orbital parameters, Northern
705 Hemispheric ice-sheet topography and albedo, and greenhouse gasses), and is constrained by oceanic
706 $\delta^{13}C$ and ventilation distributions[91]. The experiment described here is a transient simulation of the
707 period 19-15 ka forced by time-varying changes in orbital parameters, and Northern Hemispheric
708 ice-sheet topography and albedo but with freely evolving atmospheric CO_2 concentration and its
709 isotopic compositions. The total alkalinity is kept constant throughout the deglacial simulation.
710 "LH1-SO-SHW" includes meltwater input in the North Atlantic (0.04 Sv between 19 and 17.6 ka, and
711 0.07 Sv between 17.6 and 16.2 ka) to simulate HS1, as well as a strengthening of the Southern
712 Hemispheric westerlies in three steps at ~17.2 ka, 17 ka and 16.2 ka, and a decrease in buoyancy

forcing in the Southern Ocean at 17.6 ka and 16.2 ka. As a result, a ~28 ppm atmospheric CO_2 increase is simulated between 18.5 and 16 ka. Based on modelled surface CO_2 partial pressure and CO_2 flux calculations, it is known that the modelled atmospheric CO_2 rise is mostly driven by enhanced CO_2 release via the Southern Ocean.

Here, we investigate how DIC_{as} changed in the upper Atlantic during 17.4-16 ka. Following ref. [16], DIC_{as} for each time of 17.4 ka and 16 ka is calculated by:

$$DIC_{as} = DIC_s - ([PO_4^{3-}]_s - [PO_4^{3-}]^{mo}) \times C/[PO_4^{3-}] - \frac{1}{2} \times (ALK_s - ALK^{mo} + [NO_3^-]_s - [NO_3^-]^{mo}) - DIC_{constant} \quad -- \quad (4)$$

where the subscript "s" represents values normalized to S (= 32.13) at 17.4 ka, the superscript "mo" denotes mean ocean values at 17.4 ka, $[NO_3^-] = 16 \times [PO_4^{3-}]$, $C/[PO_4^{3-}] = 117$, and the arbitrary $DIC_{constant} = 2377.42$ to yield a global mean DIC_{as} of zero at 17.4 ka. Fig. 6a shows the Atlantic zonal mean DIC_{as} anomalies (16 ka relative to 17.4 ka) for 60°W-0°W.

As can be seen from Fig. 6, the North Atlantic remains a sink of atmospheric CO_2 (positive DIC_{as} anomalies), possibly linked to an enhanced solubility pump driven by strong cooling and declining salinity due to fresh water input. By contrast, the South Atlantic acts as a source of CO_2 to the atmosphere (negative DIC_{as} anomalies), linked to enhanced upwelling of DIC-rich (high CO_2 partial pressure) deep waters in the Antarctic Zone driven by strengthened Southern Hemisphere westerlies. These statements based on DIC_{as} are supported by surface water CO_2 partial pressure and CO_2 flux

734 calculations[29], lending credence for using DIC_{as} to infer air-sea CO_2 exchanges between the ocean and
735 the atmosphere.
736
737 **Bølling onset signals.** Due to potential complications (e.g., bioturbation) associated with marine
738 sediment reconstructions, it is necessary to be cautious when interpreting short-lived signals.
739 However, the fidelity of our reconstructed GGC90 $[CO_3^{2-}]_{as}$ rise at the Bølling onset is supported by
740 several lines of evidence. First, we rely on the trends obtained from Monte-Carlo and Rampfit
741 analyses, instead of individual measurements (Fig. 5c; Extended Data Fig. 6). The $[CO_3^{2-}]_{as}$ rise at the
742 Bølling onset is well defined by multiple datapoints before, during, and after the transition. Given the
743 short duration (~200 years) of the transition, it is fortuitous that we obtained three data points to define
744 the $[CO_3^{2-}]_{as}$ rise, which is based on **paired** $[CO_3^{2-}]$ and $[PO_4^{3-}]$ reconstructions (Methods). Second, if
745 taking bioturbation into account, the $[CO_3^{2-}]_{as}$ rise may have occurred over shorter time and with a
746 greater $[CO_3^{2-}]_{as}$ magnitude. Thus, our current estimate of the signal magnitude is likely conservative.
747 Also, we note the success of using sediment cores with comparable or even lower sedimentation rates
748 to investigate centennial events[9,10,92,93]. Similar to our work, previous studies had only a couple of data
749 points during the Bølling onset, which is a natural consequence associated with the abrupt event.
750 Third, our inferred AAIW expansion at the Bølling onset is supported by published proxy and model
751 results[33,39-43] (Fig. 5; Extended Data Figs. 7-9), lending credence to the robustness of our $[CO_3^{2-}]_{as}$
752 reconstructions.
753
754 **Carbon budget estimates at the Bølling onset.** The effect of AAIW expansion to raise atmospheric
755 CO_2 includes two parts: (i) decreasing DIC_{as} in the upper Atlantic and (ii) decreasing DIC_{as} of NADW

and thereby DIC_{as} of the large oceanic volume that NADW ventilates. The effect from (i) can be estimated as follows. The total atmospheric CO_2 storage reduction in the upper Atlantic ($\Delta\sum C$) is calculated by: $\Delta\sum C = V \times density \times \Delta DIC_{as} \times 12$, where V is the water mass volume experienced CO_2 loss and is estimated to be 1.9×10^{16} m^3 (assuming 50% of waters at 0.6-1.2 km and 50°S-60°N in the Atlantic), density = 1027.8 kg/m^3 (ref. [20]), and the number 12 converts C from moles into weight. Today, AAIW is found at ~500-1200 m[94] and distributed across most of the Atlantic up to ~30°N[95]. Based on ΔDIC_{as} of ~33 μmol/kg as reconstructed from GGC90 (Fig. 5c), we obtain total $\Delta\sum C$ change of ~8 PgC. Using a factor of 2.1 PgC per ppm CO_2, the air-sea CO_2 storage change in the upper Atlantic corresponds to ~4 ppm atmospheric CO_2 increase, accounting for ~1/3 of the observed atmospheric CO_2 rise.

The effect from (ii) is difficult to assess because we cannot easily quantify AAIW's impact on DIC_{as} change associated with NADW. Because AAIW is a weak water mass at sequestering atmospheric CO_2, more AAIW production would cause more CO_2 release. The total amount of CO_2 released due to an increased production of AAIW may be calculated by: $\Delta\sum C = \Delta Sv \times t \times density \times \Delta DIC_{as} \times 12$, where ΔSv is the increase in AAIW production rate over the duration (t) of the Bølling onset. This calculation provides an estimate of AAIW's influences on atmospheric CO_2 from both (i) and (ii). Model data (Fig. 5e)[43] show a pulse of increased AAIW production by ~7 Sv (ΔSv) over ~200 years (t). The ~200-year duration is also revealed by the high-resolution ice-core CO_2 record[1]. Using ΔDIC_{as} of 33 μmol/kg based on GGC90 reconstructions, we obtain a $\Delta\sum C$ of 18 PgC, corresponding to ~8 ppm change in atmospheric CO_2.

We acknowledge potentially large uncertainties associated with our calculations due to poor geographic coverage of proxy data and assumptions with the AAIW production rate. Nevertheless, our calculations indicate that AAIW variations could have played an indispensable role in driving up atmospheric CO_2 at the Bølling onset. Additional proxy data and employment of models are required to better quantify AAIW's effects on atmospheric CO_2.

Data availability

All new data are archived in PANGAEA (XX) and also provided in Supplementary Data.

References used for Methods

51 Khatiwala, S., Schmittner, A. & Muglia, J. Air-sea disequilibrium enhances ocean carbon storage during glacial periods. *Sci Adv* **5**, doi:ARTN eaaw4981, 10.1126/sciadv.aaw4981 (2019).

52 Sigman, D. M. & Boyle, E. A. Glacial/interglacial variations in atmospheric carbon dioxide. *Nature* **407**, 859-869 (2000).

53 Hain, M. P., Sigman, D. M. & Haug, G. H. in *Treatise on Geochemistry 2nd edition* doi: 10.1016/B1978-1010-1008-095975-095977.000618-095975 (2013).

54 Wang, X. T. *et al.* Deep-sea coral evidence for lower Southern Ocean surface nitrate concentrations during the last ice age. *Proceedings of the National Academy of Sciences* **114**, 3352-3357, doi:10.1073/pnas.1615718114 (2017).

55 Jaccard, S. L., Galbraith, E. D., Martinez-Garcia, A. & Anderson, R. F. Covariation of deep Southern Ocean oxygenation and atmospheric CO_2 through the last ice age. *Nature*, doi:10.1038/nature16514 (2016).

56 Anderson, R. F. *et al.* Deep-sea oxygen depletion and ocean carbon sequestration during the last ice age. *Glob. Biogeochem. Cycle* **33**, doi:10.1029/2018GB006049, doi:doi:10.1029/2018GB006049 (2019).

57 Galbraith, E. D. & Skinner, L. C. The Biological Pump During the Last Glacial Maximum. *Annu Rev Mar Sci* **12**, 559-586, doi:10.1146/annurev-marine-010419-010906 (2020).

58 Ito, T. & Follows, M. J. Preformed phosphate, soft tissue pump and atmospheric CO2. *Journal of Marine Research* **63**, 813-839, doi:Doi 10.1357/0022240054663231 (2005).

59 Ito, T., Follows, M. J. & Boyle, E. A. Is AOU a good measure of respiration in the oceans? *Geophysical Research Letters* **31**, doi:Artn L17305, 10.1029/2004gl020900 (2004).

60 Gruber, N. *et al.* The oceanic sink for anthropogenic CO2 from 1994 to 2007. *Science* **363**, 1193-+, doi:10.1126/science.aau5153 (2019).
61 Toggweiler, J. R., Gnanadesikan, A., Carson, S., Murnane, R. & Sarmiento, J. L. Representation of the carbon cycle in box models and GCMs: 1. Solubility pump. *Glob. Biogeochem. Cycle* **17**, doi:10.1029/2001gb001401, doi:10.1029/2001gb001401 (2003).
62 Toggweiler, J. R., Murnane, R., Carson, S., Gnanadesikan, A. & Sarmiento, J. L. Representation of the carbon cycle in box models and GCMs: 2. Organic pump. *Glob. Biogeochem. Cycle* **17**, doi:10.1029/2001gb001841, doi:10.1029/2001gb001841 (2003).
63 Broecker, W. S. & Peng, T. H. The role of $CaCO_3$ compensation in the glacial to interglacial atmospheric CO_2 change. *Glob. Biogeochem. Cycle* **1**, 15-29 (1987).
64 Sortor, R. N. & Lund, D. C. No evidence for a deglacial intermediate water Delta C-14 anomaly in the SW Atlantic. *Earth Planet. Sci. Lett.* **310**, 65-72, doi:DOI 10.1016/j.epsl.2011.07.017 (2011).
65 Stuiver, M. & Reimer, P. J. Extended 14C Data Base and Revised CALIB 3.0 14C Age Calibration Program. *Radiocarbon* **35**, 215-230, doi:10.1017/s0033822200013904 (1993).
66 Reimer, P. J. *et al.* IntCal13 and Marine13 Radiocarbon Age Calibration Curves 0–50,000 Years cal BP. *Radiocarbon* **55**, 1869-1887, doi:10.2458/azu_js_rc.55.16947 (2013).
67 Ramsey, C. B. Deposition models for chronological records. *Quat. Sci. Rev.* **27**, 42-60, doi:10.1016/j.quascirev.2007.01.019 (2008).
68 Barker, S., Greaves, M. & Elderfield, H. A study of cleaning procedures used for foraminiferal Mg/Ca paleothermometry. *Geochem. Geophys. Geosyst.* **4**, doi:10.1029/2003GC000559, doi:doi:10.1029/2003GC000559 (2003).
69 Rosenthal, Y., Boyle, E. A. & Slowey, N. Temperature control on the incorporation of magnesium, strontium, fluorine, and cadmium into benthic foraminiferal shells from Little Bahama Bank: Prospects for thermocline paleoceanography. *Geochim. Cosmochim. Acta* **61**, 3633-3643 (1997).
70 Yu, J. M., Day, J., Greaves, M. & Elderfield, H. Determination of multiple element/calcium ratios in foraminiferal calcite by quadrupole ICP-MS. *Geochem. Geophys. Geosyst.* **6**, Q08P01, doi:10.1029/2005GC000964 (2005).
71 Waelbroeck, C. *et al.* The timing of the last deglaciation in North Atlantic climate records. *Nature* **412**, 724-727, doi:Doi 10.1038/35089060 (2001).
72 Stern, J. V. & Lisiecki, L. E. North Atlantic circulation and reservoir age changes over the past 41,000years. *Geophysical Research Letters* **40**, 3693-3697, doi:10.1002/grl.50679 (2013).
73 Yu, J. *et al.* Responses of the deep ocean carbonate system to carbon reorganization during the Last Glacial–interglacial cycle. *Quat. Sci. Rev.* **76**, 39-52, doi:http://dx.doi.org/10.1016/j.quascirev.2013.06.020 (2013).
74 Oppo, D. *et al.* Data Constraints on Glacial Atlantic Water Mass Geometry and Properties. *Paleoceanography and Paleoclimatology* **33**, 1013-1034, doi:10.1029/2018PA003408 (2018).
75 Boyle, E. A. Cadmium: Chemical tracer of deepwater paleoceanography. *Paleoceanogr.* **3**, 471-489 (1988).
76 Boyle, E. A., Labeyrie, L. & Duplessy, J. C. Calcitic foraminiferal data confirmed by cadmium in aragonitic Hoeglundina - application to the Last Glacial Maximum in the northern Indian Ocean. *Paleoceanogr.* **10**, 881-900 (1995).

77 Marchitto, T. & Broecker, W. Deep water mass geometry in the glacial Atlantic Ocean: A review of constraints from the paleonutrient proxy Cd/Ca. *Geochem. Geophys. Geosyst.* **7**, doi:10.1029/2006GC001323 (2006).
78 Elderfield, H. & Rickaby, R. E. M. Oceanic Cd/P ratio and nutrient utilization in the glacial Southern Ocean. *Nature* **405**, 305-310 (2000).
79 Lear, C. H. *et al.* Breathing more deeply: Deep ocean carbon storage during the mid-Pleistocene climate transition. *Geology* **44**, 1035-1038, doi:10.1130/G38636.1 (2016).
80 Farmer, J. R. *et al.* Deep Atlantic Ocean carbon storage and the rise of 100,000-year glacial cycles. *Nature Geoscience* **12**, 355-+, doi:10.1038/s41561-019-0334-6 (2019).
81 Marchitto, T. M. *et al.* Improved oxygen isotope temperature calibrations for cosmopolitan benthic foraminifera. *Geochim. Cosmochim. Acta* **130**, 1-11, doi:10.1016/j.gca.2013.12.034 (2014).
82 Lambeck, K., Rouby, H., Purcell, A., Sun, Y. Y. & Sambridge, M. Sea level and global ice volumes from the Last Glacial Maximum to the Holocene. *P Natl Acad Sci USA* **111**, 15296-15303, doi:10.1073/pnas.1411762111 (2014).
83 Stanford, J. D. *et al.* Timing of meltwater pulse 1a and climate responses to meltwater injections. *Paleoceanogr.* **21**, doi: 10.1029/2006pa001340, doi:Artn Pa4103, 10.1029/2006pa001340 (2006).
84 Waelbroeck, C. *et al.* Sea-level and deep water temperature changes derived from benthic foraminifera isotopic records. *Quat. Sci. Rev.* **21**, 295-305 (2002).
85 Galbraith, E. D. & Martiny, A. C. A simple nutrient-dependence mechanism for predicting the stoichiometry of marine ecosystems. *P Natl Acad Sci USA* **112**, 8199-8204, doi:10.1073/pnas.1423917112 (2015).
86 Anderson, L. A. & Sarmiento, J. L. Redfield ratios of remineralization determined by nutrient data-analysis. *Glob. Biogeochem. Cycle* **8**, 65-80, doi:Doi 10.1029/93gb03318 (1994).
87 Grant, K. M. *et al.* Rapid coupling between ice volume and polar temperature over the past 150,000 years. *Nature* **491**, 744-747, doi:doi:10.1038/nature11593 (2012).
88 Rohling, E. J. *et al.* Sea-level and deep-sea-temperature variability over the past 5.3 million years. *Nature* **508**, 477-482, doi:Doi 10.1038/Nature13230 (2014).
89 Mudelsee, M. Ramp function regression: a tool for quantifying climate transitions. *Computers & Geosciences* **26**, 293-307, doi:https://doi.org/10.1016/S0098-3004(99)00141-7 (2000).
90 Goosse, H. *et al.* Description of the Earth system model of intermediate complexity LOVECLIM version 1.2. *Geosci Model Dev* **3**, 603-633, doi:DOI 10.5194/gmd-3-603-2010 (2010).
91 Menviel, L. *et al.* Poorly ventilated deep ocean at the Last Glacial Maximum inferred from carbon isotopes: A data-model comparison study. *Paleoceanogr.* **31**, doi:10.1002/2016PA003024, doi:doi:10.1002/2016PA003024. (2017).
92 Gottschalk, J. *et al.* Glacial heterogeneity in Southern Ocean carbon storage abated by fast South Indian deglacial carbon release. *Nat Commun* **11**, doi:ARTN 6192, 10.1038/s41467-020-20034-1 (2020).
93 Thornalley, D. J. R., Barker, S., Broecker, W., Elderfield, H. & McCave, I. N. The Deglacial Evolution of North Atlantic Deep Convection. *Science* **331**, 202-205 (2011).
94 Talley, L. D. in *The South Atlantic* (Springer, 1996).

95 Liu, M. & Tanhua, T. Water masses in the Atlantic Ocean: characteristics and distributions. *Ocean Sci* **17**, 463-486, doi:10.5194/os-17-463-2021 (2021).
96 Yu, J. *et al.* Loss of carbon from the deep sea since the Last Glacial Maximum. *Science* **330**, 1084-1087, doi: 1010.1126/science.1193221 (2010).
97 Farrell, J. W. & Prell, W. L. Climatic change and $CaCO_3$ preservation: an 800,000 year bathymetric reconstruction from the central equatorial Pacific Ocean. *Paleoceanogr.* **4**, 447-466 (1989).
98 Farrell, J. W. & Prell, W. L. Pacific $CaCO_3$ preservation and $\delta^{18}O$ since 4 Ma: paleoceanic and paleoclimatic implications. *Paleoceanogr.* **6**, 485-498 (1991).
99 Kohler, P. & Munhoven, G. Late Pleistocene Carbon Cycle Revisited by Considering Solid Earth Processes. *Paleoceanography and Paleoclimatology* **35**, doi:ARTN e2020PA004020, 10.1029/2020PA004020 (2020).
100 Chase, Z., Anderson, R. F., Fleisher, M. Q. & Kubik, P. W. Accumulation of biogenic and lithogenic material in the Pacific sector of the Southern Ocean during the past 40,000 years. *Deep-Sea Research Part Ii-Topical Studies in Oceanography* **50**, 799-832, doi:Pii S0967-0645(02)00595-7, Doi 10.1016/S0967-0645(02)00595-7 (2003).
101 Shao, J. *et al.* Atmosphere-Ocean CO2 Exchange Across the Last Deglaciation From the Boron Isotope Proxy. *Paleoceanography and Paleoclimatology* **34**, 1650-1670, doi:https://doi.org/10.1029/2018PA003498 (2019).
102 Poppelmeier, F. *et al.* Influence of Ocean Circulation and Benthic Exchange on Deep Northwest Atlantic Nd Isotope Records During the Past 30,000 Years. *Geochem. Geophys. Geosyst.* **20**, 4457-4469, doi:10.1029/2019gc008271 (2019).
103 Roberts, N. L. & Piotrowski, A. M. Radiogenic Nd isotope labeling of the northern NE Atlantic during MIS 2. *Earth Planet. Sci. Lett.* **423**, 125-133, doi:https://doi.org/10.1016/j.epsl.2015.05.011 (2015).
104 Zhao, N. *et al.* Glacial-interglacial Nd isotope variability of North Atlantic Deep Water modulated by North American ice sheet (vol 56, pg 313, 2019). *Nat Commun* **11**, doi:ARTN 3374, 10.1038/s41467-020-17208-2 (2020).
105 Piotrowski, A. *et al.* Reconstructing deglacial North and South Atlantic deep water sourcing using foraminiferal Nd isotopes. *Earth Planet. Sci. Lett.* **357-358**, 289-297 (2012).
106 Skinner, L. C. *et al.* North Atlantic versus Southern Ocean contributions to a deglacial surge in deep ocean ventilation. *Geology* **41**, 667-670, doi:10.1130/G34133.1 (2013).
107 Wilson, D. J. *et al.* Sea-ice control on deglacial lower cell circulation changes recorded by Drake Passage deep-sea corals. *Earth Planet. Sci. Lett.* **544**, doi:ARTN 116405, 10.1016/j.epsl.2020.116405 (2020).
108 Howe, J. N. W., Piotrowski, A. M. & Rennie, V. C. F. Abyssal origin for the early Holocene pulse of unradiogenic neodymium isotopes in Atlantic seawater. *Geology* **44**, 831-834, doi:10.1130/G38155.1 (2016).
109 Du, J. H., Haley, B. A. & Mix, A. C. Evolution of the Global Overturning Circulation since the Last Glacial Maximum based on marine authigenic neodymium isotopes. *Quat. Sci. Rev.* **241**, doi:ARTN 106396, 10.1016/j.quascirev.2020.106396 (2020).
110 Valley, S., Lynch-Stieglitz, J. & Marchitto, T. M. Timing of Deglacial AMOC Variability From a High-Resolution Seawater Cadmium Reconstruction. *Paleoceanogr.* **32**, 1195-1203, doi:10.1002/2017pa003099 (2017).

111 Xie, R. F. C., Marcantonio, F. & Schmidt, M. W. Deglacial variability of Antarctic Intermediate Water penetration into the North Atlantic from authigenic neodymium isotope ratios. *Paleoceanogr.* **27**, doi:Artn Pa3221, 10.1029/2012pa002337 (2012).
112 Xie, R. F. C., Marcantonio, F. & Schmidt, M. W. Reconstruction of intermediate water circulation in the tropical North Atlantic during the past 22,000 years. *Geochim. Cosmochim. Acta* **140**, 455-467, doi:10.1016/j.gca.2014.05.041 (2014).

Extended Data Fig. 1 | Preindustrial Atlantic $[CO_3^{2-}]_{as}$ vs DIC_{as} as shown in Fig. 1. Data are from ref. [1], based on the calculation method from ref. [2]. Black curve represents the best fit of the data. Simply put, when a water mass sequesters more atmospheric CO_2, it has lower $[CO_3^{2-}]_{as}$ and higher DIC_{as}, and *vice versa*. For example, adding CO_2 into a package of water would increase its DIC_{as}. At the same time, because the added CO_2 would convert some $[CO_3^{2-}]_{as}$ into bicarbonate, its $[CO_3^{2-}]_{as}$ should decrease. Thus, the negative $[CO_3^{2-}]_{as}$–DIC_{as} correlation is exactly expected from the CO_2 system theory[3]. See ref. [2] and Methods for detailed discussions.

Extended Data Fig. 2 | $[CO_3^{2-}]_{as}/DIC_{as}$ sensitivity vs. $[CO_3^{2-}]_{Norm}$. $[CO_3^{2-}]_{Norm} = [CO_3^{2-}]_{as} + 78$. The sensitivity is calculated based on the method from ref. [2]. The large circle indicates the average sensitivity (-0.48) for $[CO_3^{2-}]_{Norm}$ ranges (shaded region) observed at sites GGC90 and NEAP 4K during the last deglaciation.

Extended Data Fig. 3 | Effect of biogenic composition and global alkalinity change on GGC90 $[CO_3^{2-}]_{as}$. a, Biogenic composition effect. C/$[PO_4^{3-}]$ and R values represent Redfield ratio and rain ratio (i.e., molar carbon ratio between soft and skeleton parts), respectively. **b-d**, Effect of global alkalinity (ALK) changes associated with carbonate compensation. Assuming little change in continental weathering, increased carbonate burial in the deep ocean[10-13] and on shelves driven by sea level rise[14-16] would decrease the global ALK (**b**) and DIC at a 2:1 ratio during the last deglaciation. These changes would lower seawater $[CO_3^{2-}]_{as}$ (**c**), even without any air-sea CO_2 exchange. Taken this global ALK effect into account, $[CO_3^{2-}]_{as}$ at GGC90 would show a larger increase during the last deglacial (**d**), suggesting greater CO_2 outgassing from the upper Atlantic. Here we use a recent model-based global ALK change[17] to demonstrate the global ALK effect. Using other ALK estimates may yield different amplitudes of $[CO_3^{2-}]_{as}$ changes, but the overall pattern should maintain. Due to the large and slow response of the global oceanic ALK reservoir, any global ALK change would affect $[CO_3^{2-}]_{as}$ would be gradual (**c**). As can be seen, even considering potential influences from biogenic composition and global ALK changes, deglacial $[CO_3^{2-}]_{as}$ evolution pattern persists, supporting our interpretation in the main text.

Extended Data Fig. 4 | Antarctic Zone opal flux data from different sectors of the Southern Ocean. As can be seen, opal fluxes differ in absolute values (e.g., much higher deglacial fluxes in the Atlantic sector core 13PC than in other cores) and patterns (e.g., a substantial decline in the Atlantic core 13PC during Bølling/Allerød, which is not seen in other cores; sustained opal flux increase in PS75/072-4 during the Holocene, but not seen in other cores). These different patterns may reflect varying hydrological conditions between different sectors of the Southern Ocean. This warrants the use of additional proxies to check palaeoceanographic inferences based on opal fluxes. Opal flux data are from refs. [18-20]. Literature data are plotted against their originally published age models.

Extended Data Fig. 5 | Heterogeneous surface-water CO_2 partial pressure (pCO_2) in the Southern Ocean. a, Spatial surface-water pCO_2 during the preindustrial, based on the GLODAP data set[1]. Note that the data coverage is incomplete and should not be treated to reflect the annual mean conditions. **b**, Temporal surface water and atmospheric pCO_2 gradient (ΔpCO_2) at PS2498-1 from the South Atlantic. **c**, Temporal ΔpCO_2 at MD97-2106 from the South Pacific (see also ref. [21]). Surface-water pCO_2 was heterogeneous in the Southern Ocean, both spatially and temporally. Despite the Southern Ocean being an overall source of CO_2 to the atmosphere, some surface ocean regions had lower pCO_2 than the atmosphere, possibly reflecting seasonal and hydrographical variations in surface conditions. When using surface data, this highlights the need to obtain data for different seasons at broad locations to gain complete information about the Southern Ocean's role in atmospheric CO_2[22]. Literature data are plotted against their originally published age models.

Extended Data Fig. 6 | Concurrent changes in atmospheric CO_2 and ΔDIC_{as} in core GGC90 at the Bølling onset. a, WDC ice-core atmospheric CO_2[1]. **b**, ΔDIC_{as} in core GGC90 (this study). The ramp fittings of atmospheric CO_2 and ΔDIC_{as} records are indicated in gray and red lines, respectively. The estimated change-points ($\pm$standard errors) of the CO_2 transition are: t_1 (start) = 14.77$\pm$0.04 ka, t_2 (end) = 14.63$\pm$0.03 ka. The estimated change-points ($\pm$standard errors) of the ΔDIC_{as} transition are: t_1 (start) = 14.89$\pm$0.35 ka, t_2 (end) = 14.53$\pm$0.34 ka. Note that the large errors with ΔDIC_{as} change-point dates are mainly sourced from the assumed uncertainties ($\pm$200 years) associated with surface reservoir ages used for age model constructions (Methods). The slightly broader ramp in ΔDIC_{as} at GGC90 is expected due to bioturbation. The results are based on 1,000 bootstrap replications. The black dash lines highlight the concurrence of the atmospheric and oceanic transitions. The analyses are based on Rampfit software[39].

Extended Data Fig. 7 | Increased AAIW mixing at GGC90 at the Bølling onset. a, Core locations against modern seawater salinity[1]. **b**, Pa/Th[23]. Everything else being equal, NADW invigoration at the Bølling onset (vertical yellow bar) would decrease εNd at GGC90. To prevent any εNd decline at GGC90, a concomitant increase in AAIW production would be required. **c**, GGC90 εNd[24] compared with records from high latitudes North [eastern basin: BOFS 17K[25]; western basin: KNR198 cores[26]] and South [curves: TNO57-21[27] and MD07-3076Q[28]; circles: deep-sea corals[29]] Atlantic. At the Bølling onset, GGC90 εNd shifted towards southern-sourced water (SSW) compositions (light blue shading), suggesting more AAIW mixing. **d**, Deep Atlantic εNd[26] became even less radiogenic than shallower water εNd (grey shading), possibly linked to enhanced weathering of the North America[26]. **e**, Authigenic εNd at the Blake Bahama Outer Ridge[24]. In **d** and **e**, εNd declines at the Bølling onset possibly suggest addition of less radiogenic εNd during the southward transport of NADW[24,26,30]. This effect [e.g., non-conservativeness during mixing[31]] would require even more AAIW mixing to maintain radiogenic εNd at GGC90 at the Bølling onset. Grey and light blue bars along y-axes indicate modern northern-sourced water (NSW) and SSW endmembers, respectively. These endmembers are thought to have changed in the past[25,26,30]. Literature data are plotted against their originally published age models.

Extended Data Fig. 8 | Northward AAIW expansion at the Bølling onset. a, Core locations against the modern seawater [PO_4^{3-}] (shading)[1]. Solid and dashed white curves show, respectively, inferred AAIW geometries for HS1 and the Bølling onset, based on proxy and model results [$\delta^{13}C$[32,33], εNd[34-36], Cd/Ca[37,38], and model[39]]. More data are needed to better constrain these geometries. **b**, Pa/Th at GGC5[23]. **c**, Benthic Cd/Ca for the mid-depth Atlantic[5,37,38, this study]. At NEAP 4K, *C. wuellerstorfi* Cd/Ca are adjusted by a factor of 2.2 to account for D_{Cd} difference between *H. elegans* and *C. wuellerstorfi*[9,40]. Vertical band shows the Bølling onset at ~14.7 ±0.25 ka. Compared to 26JPC (grey circles), NEAP 4K (blue circles) and GGC100 (blue squares) are more affected by NADW due to their deeper water depths and higher latitudinal locations (**a**). Without increased AAIW mixing, enhanced production of low-Cd NADW would have lowered Cd at 26JPC. Additionally, enhanced ventilation by

NADW would decrease respired nutrient and thereby lower Cd at 26JPC. Thus, the sustained high Cd at 26JPC (and NEAP 4K) suggests increased mixing of AAIW at intermediate depths of the tropical North Atlantic at the Bølling onset, which is also supported by εNd data shown in Extended Data Fig. 9. Literature data are plotted against their originally published age models.

Extended Data Fig. 9 | Increased AAIW mixing at the intermediate North Atlantic at the Bølling onset. a, Core locations against modern seawater salinity[1]. **b**, Pa/Th, a proxy for NADW strength[23]. **c**, εNd at 26 JPC [discrete and connected circles are based on fish teeth and Fe-Mn leachates, respectively[41,42]]. Grey and light blue shadings and blue circles are defined in Extended Data Fig. 7. εNd at 26JPC was well within the range of NSW values (grey shading) during HS1, but shifted towards SSW values (light blue shading) at the Bølling onset. This is consistent with a northward expansion of AAIW at the Bølling onset[33,37-39]. Vertical grey and light blue bars along y-axis indicate modern NSW and SSW endmembers, respectively.

Extended Data Fig. 10 | Northward transport of AAIW in the preindustrial Atlantic Ocean. a, DIC_{as}–neutral density (γ^N) transect. **b**, DIC_{as}–salinity transect. Along isopycnal surfaces (γ^N = ~27.5 kg/m^3 for AAIW), the low-DIC_{as} signals of AAIW can be traced at the intermediate depths in the high-latitude North Atlantic[26-31] (**a**). Cross-equator transport of AAIW is also suggested by the northward extension of low-salinity waters at ~1 km (**b**). AAIW is found at ~500-1200 m[32]. Latest analyses suggest AAIW is distributed across most of the Atlantic up to ~30°N[33]. Because at least part of intermediate waters in the North Atlantic would be entrained to form NADW[26-28], northward AAIW expansion would affect NADW's DIC_{as} values. At the Bølling onset, our and previous results[30,31,34-37] suggest a sudden northward expansion of AAIW (Extended Data Figs. 7-9) with an effect to lower DIC_{as} and thus atmospheric CO_2 sequestration efficiency of NADW. Map generated using Ocean Data View based on the GLODAP data set[14,38].

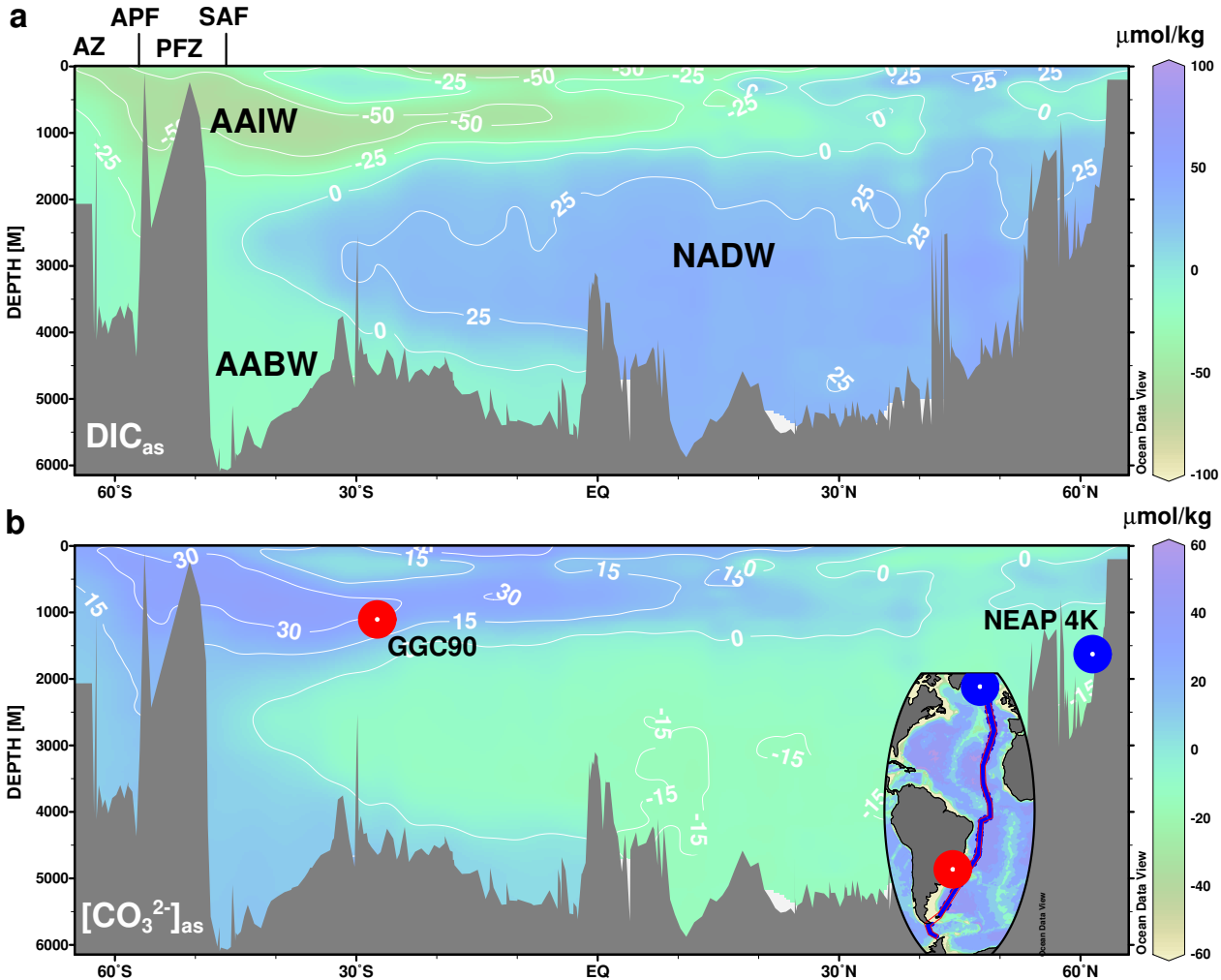
a
AZ
APF
PFZ
SAF
µmol/kg
AAIW
NADW
AABW
DIC$_{as}$
DEPTH [M]
60˚S
30˚S
EQ
30˚N
60˚N
Ocean Data View
b
µmol/kg
GGC90
NEAP 4K
[CO$_3^{2-}$]$_{as}$
DEPTH [M]
60˚S
30˚S
EQ
30˚N
60˚N
Ocean Data View

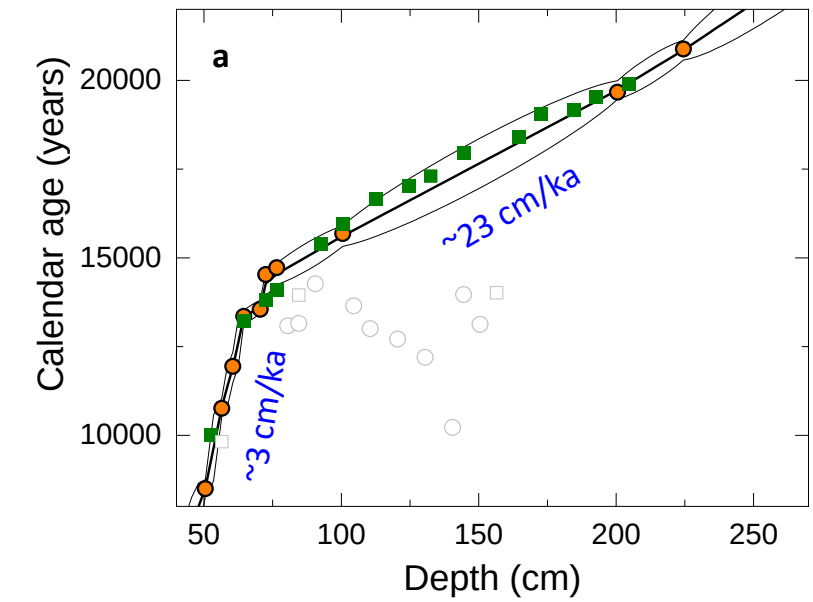
a
Calendar age (years)
20000
15000
10000
50
100
150
200
250
Depth (cm)
~3 cm/ka
~23 cm/ka

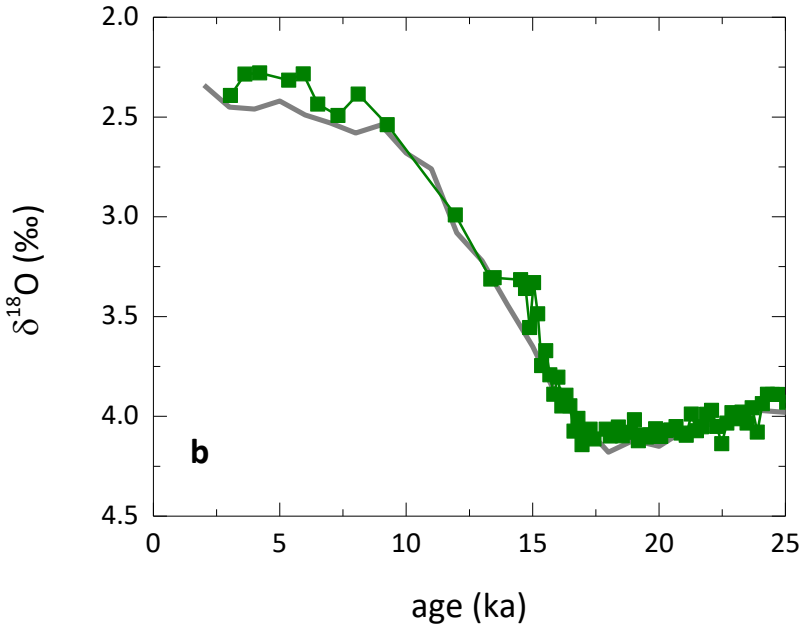
δ18O (‰)
2.0
2.5
3.0
3.5
4.0
4.5
b
0
5
10
15
20
25
age (ka)

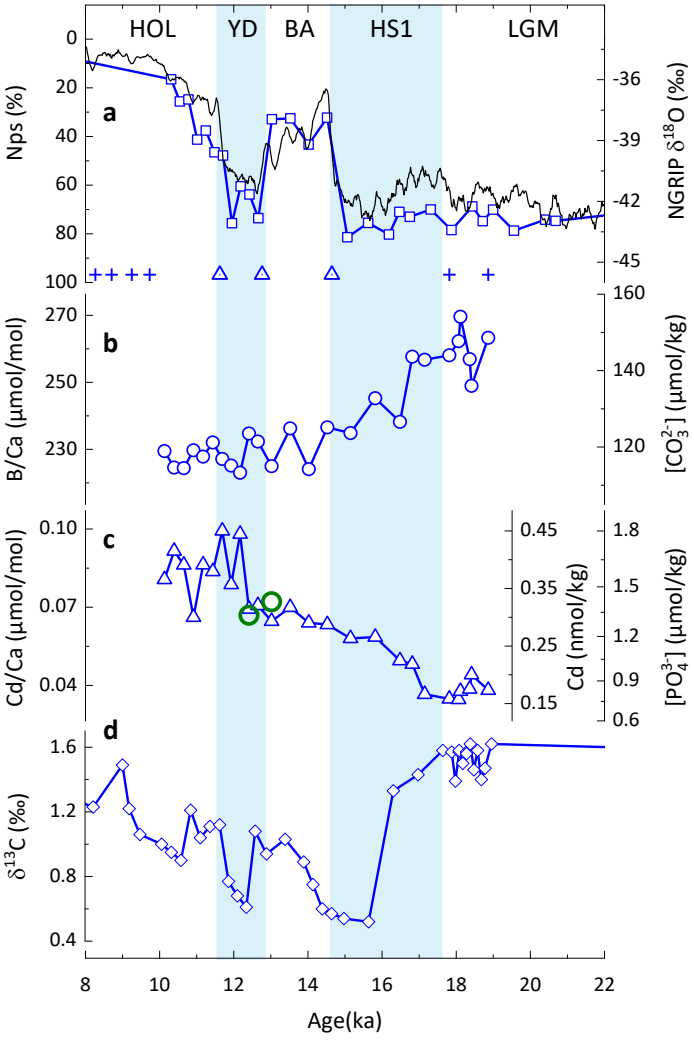
HOL
YD
BA
HS1
LGM
a
Nps (%)
NGRIP δ18O (‰)
b
B/Ca (μmol/mol)
[CO32-] (μmol/kg)
c
Cd/Ca (μmol/mol)
Cd (nmol/kg)
[PO43-] (μmol/kg)
d
δ13C (‰)
Age(ka)

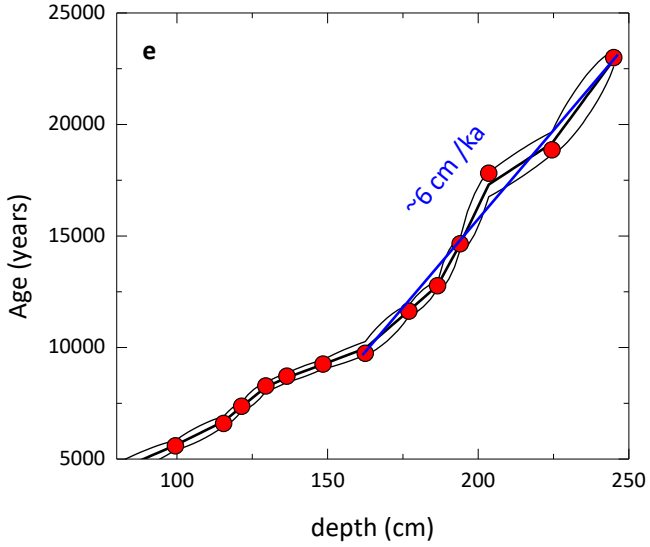
e
~6 cm /ka
Age (years)
depth (cm)

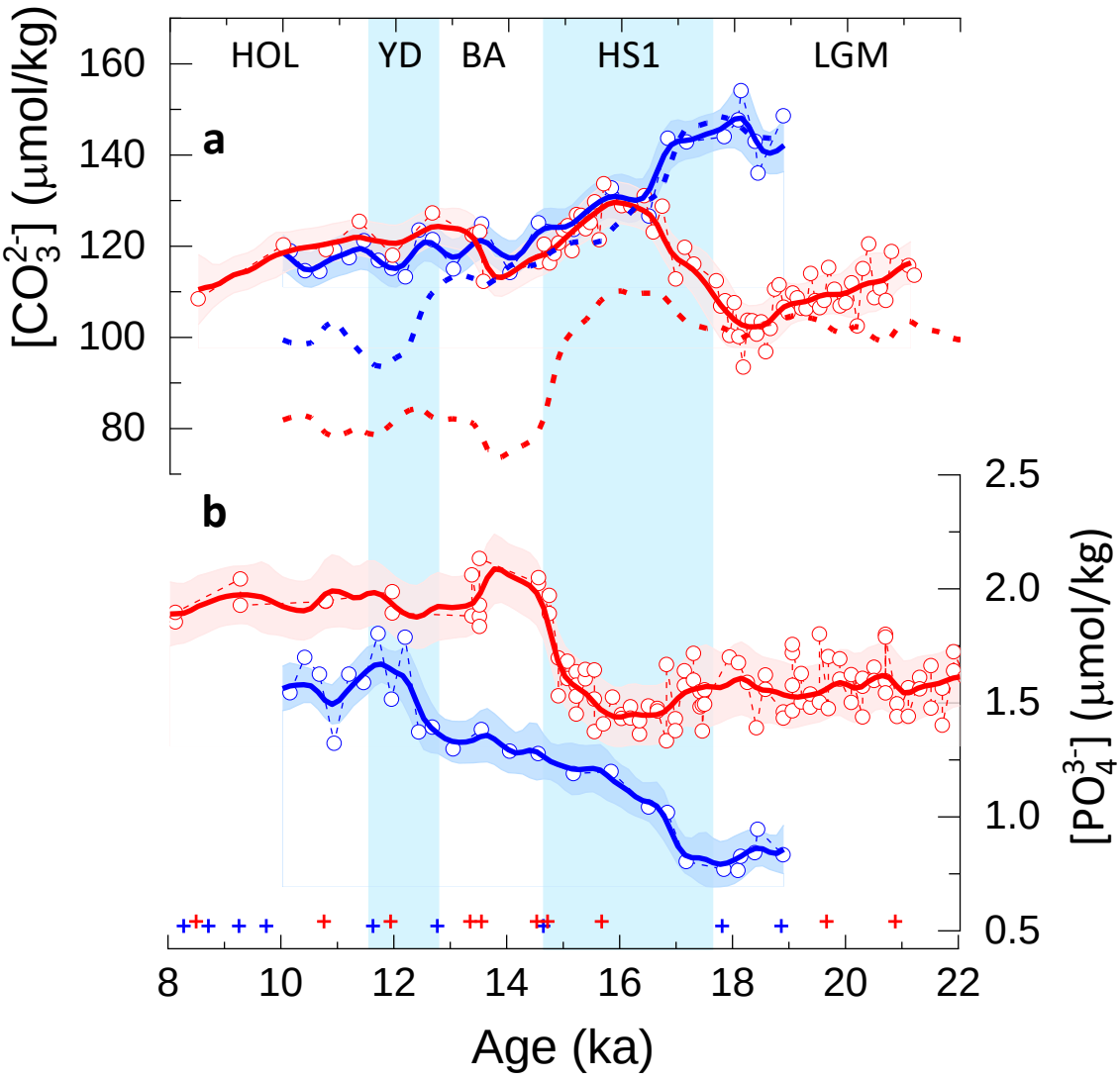
HOL
YD
BA
HS1
LGM
a
b
160
140
120
100
80
2.5
2.0
1.5
1.0
0.5
8
10
12
14
16
18
20
22
Age (ka)
[CO32-] (µmol/kg)
[PO43-] (µmol/kg)

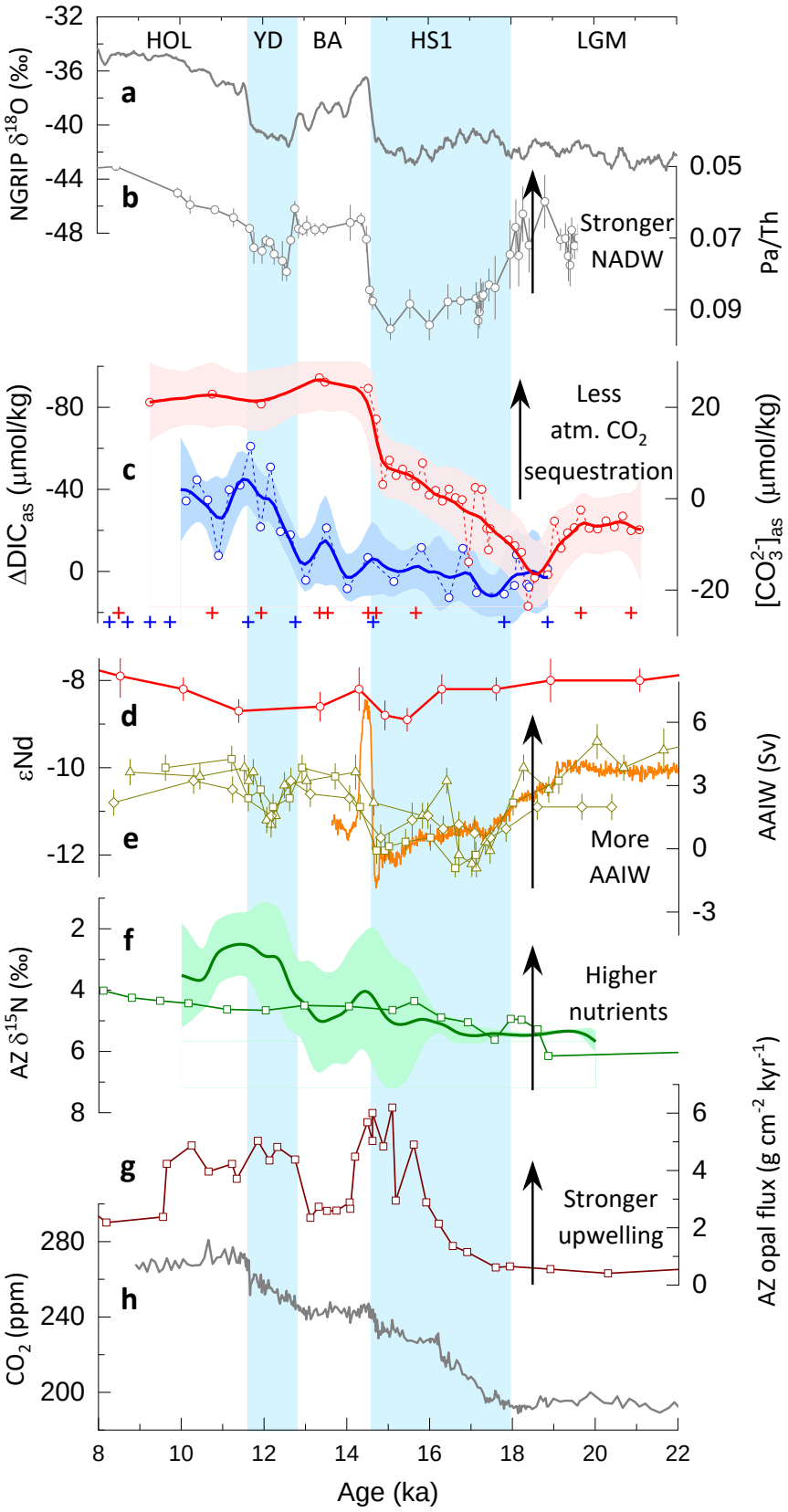
HOL
YD
BA
HS1
LGM
a
b
c
d
e
f
g
h
NGRIP δ18O (‰)
Pa/Th
Stronger NADW
ΔDICas (μmol/kg)
[CO32-]as (μmol/kg)
Less atm. CO2 sequestration
εNd
AAIW (Sv)
More AAIW
AZ δ15N (‰)
Higher nutrients
AZ opal flux (g cm-2 kyr-1)
Stronger upwelling
CO2 (ppm)
Age (ka)

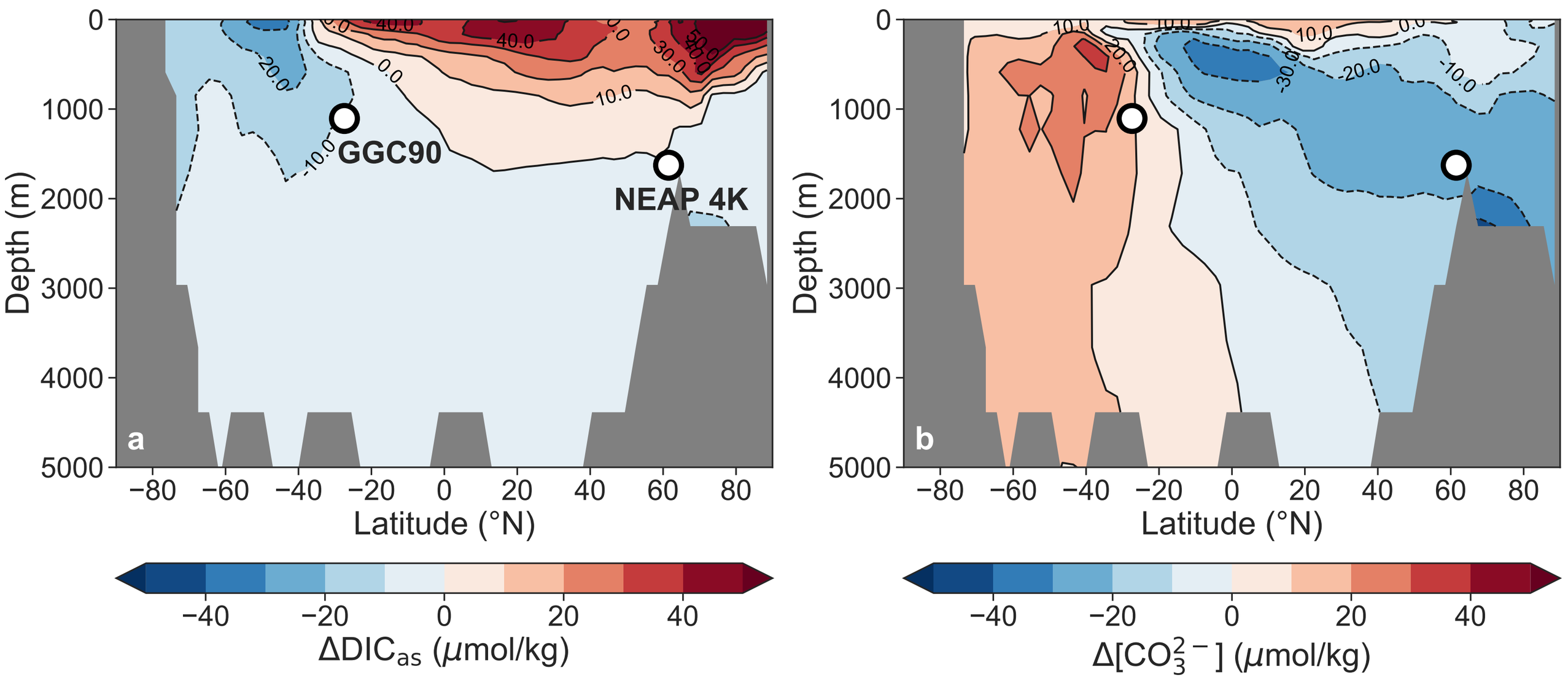
GGC90
NEAP 4K
a
b
Depth (m)
Latitude (°N)
ΔDIC$_{as}$ (μmol/kg)
Δ[CO_3^{2-}] (μmol/kg)

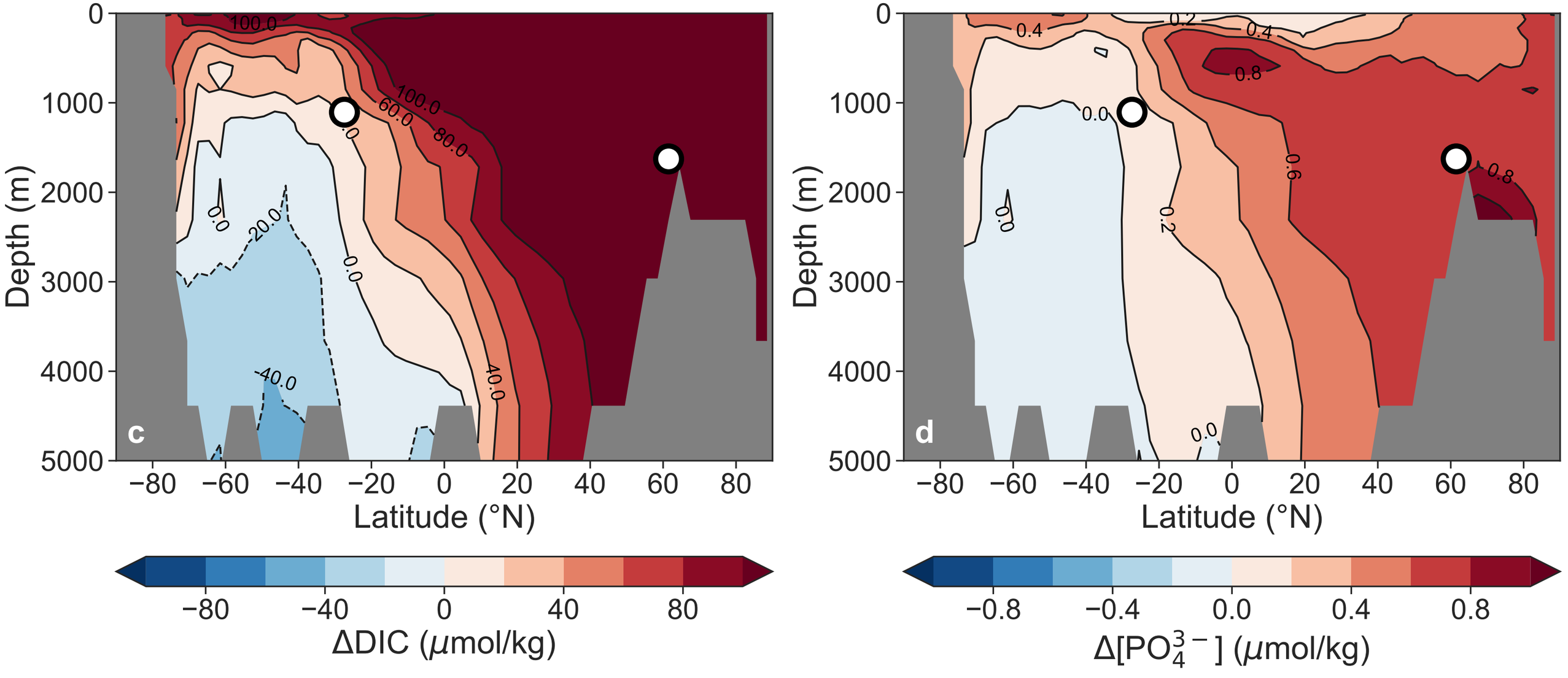
c
d
Depth (m)
Latitude (°N)
ΔDIC (μmol/kg)
Δ[PO_4^{3-}] (μmol/kg)

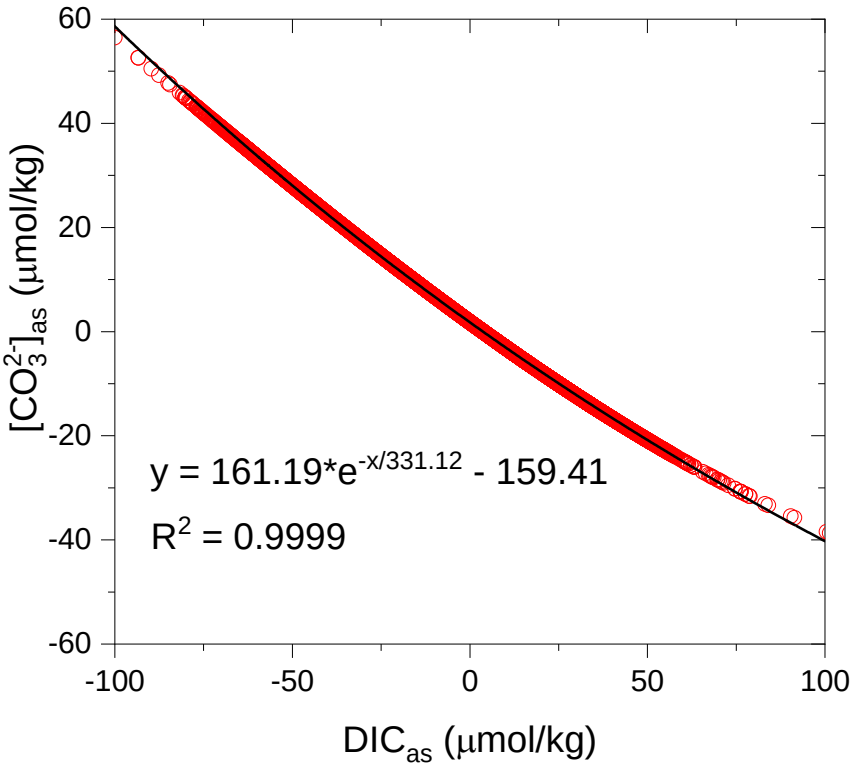
60
40
20
0
-20
-40
-60
-100
-50
0
50
100
$[CO_3^{2-}]_{as}$ (μmol/kg)
DIC_{as} (μmol/kg)
y = 161.19*e^-x/331.12 - 159.41
R^2 = 0.9999

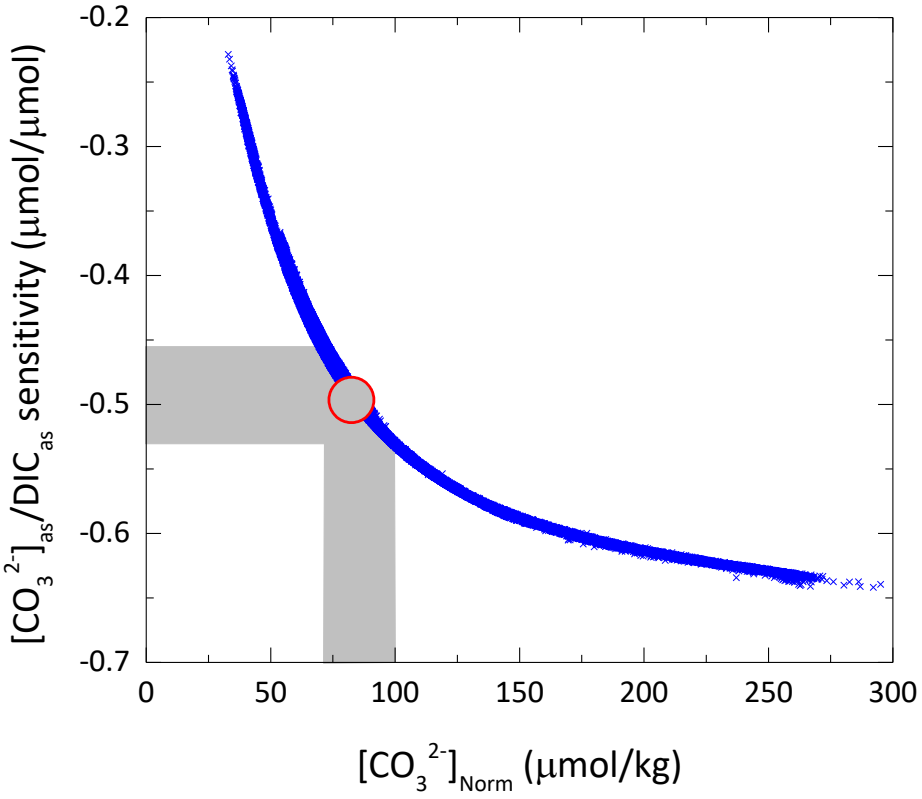
-0.2
-0.3
-0.4
-0.5
-0.6
-0.7
0
50
100
150
200
250
300
[CO3 2-]as/DICas sensitivity (µmol/µmol)
[CO3 2-]Norm (µmol/kg)

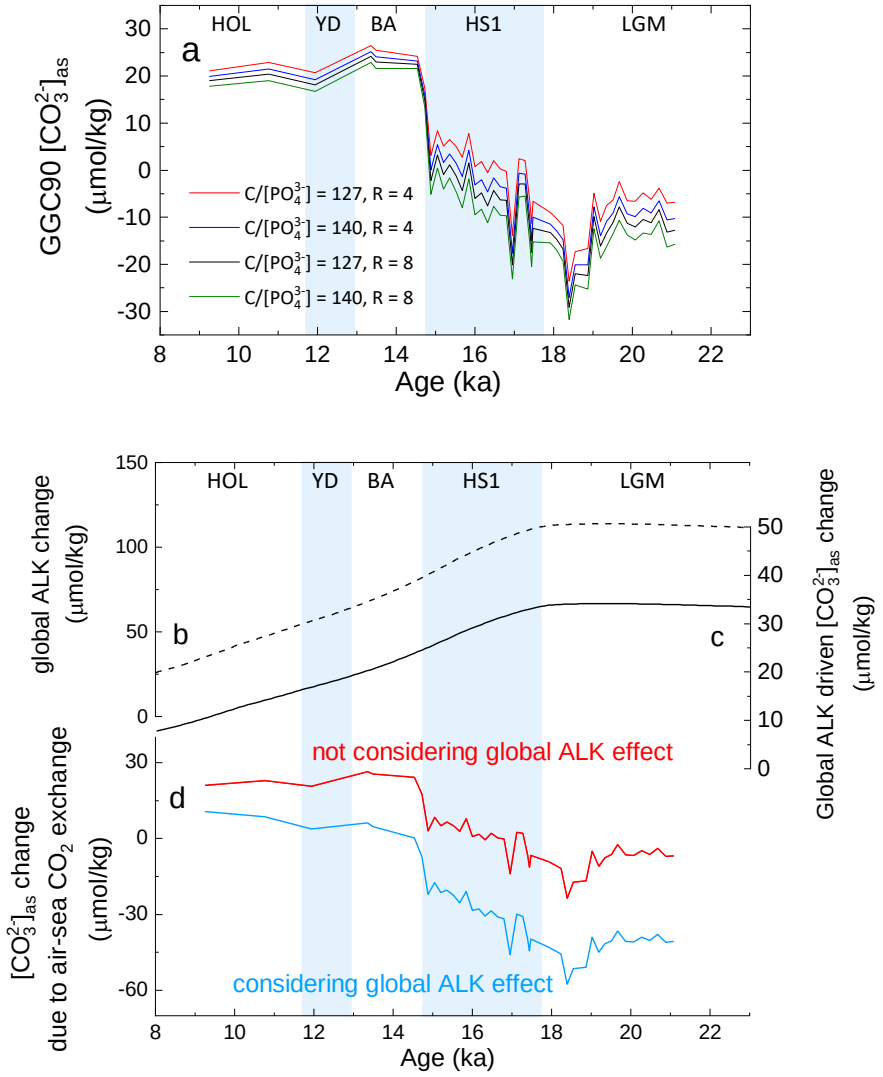
a
HOL
YD
BA
HS1
LGM
GGC90 [CO32-]las (µmol/kg)
C/[PO43-] = 127, R = 4
C/[PO43-] = 140, R = 4
C/[PO43-] = 127, R = 8
C/[PO43-] = 140, R = 8
Age (ka)
b
c
global ALK change (µmol/kg)
Global ALK driven [CO32-]las change (µmol/kg)
not considering global ALK effect
d
considering global ALK effect
[CO32-]las change due to air-sea CO2 exchange (µmol/kg)
Age (ka)

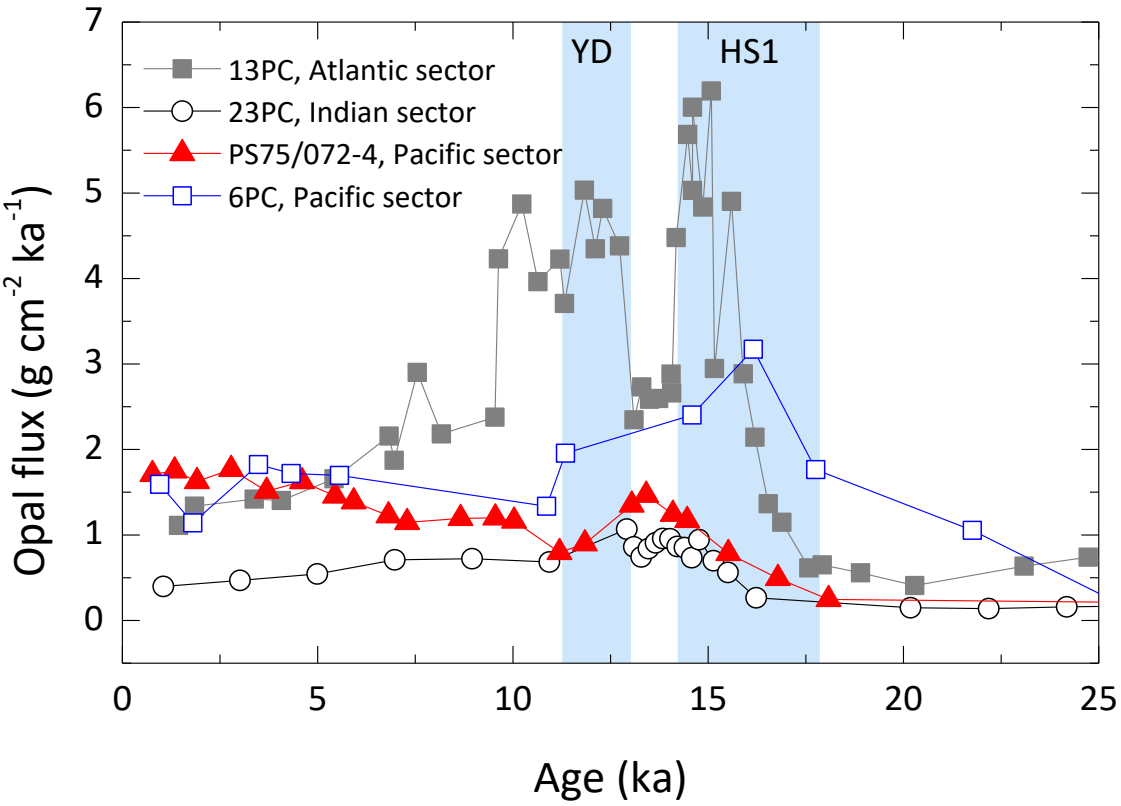
YD
HS1
13PC, Atlantic sector
23PC, Indian sector
PS75/072-4, Pacific sector
6PC, Pacific sector
Opal flux (g cm-2 ka-1)
Age (ka)
0
1
2
3
4
5
6
7
0
5
10
15
20
25

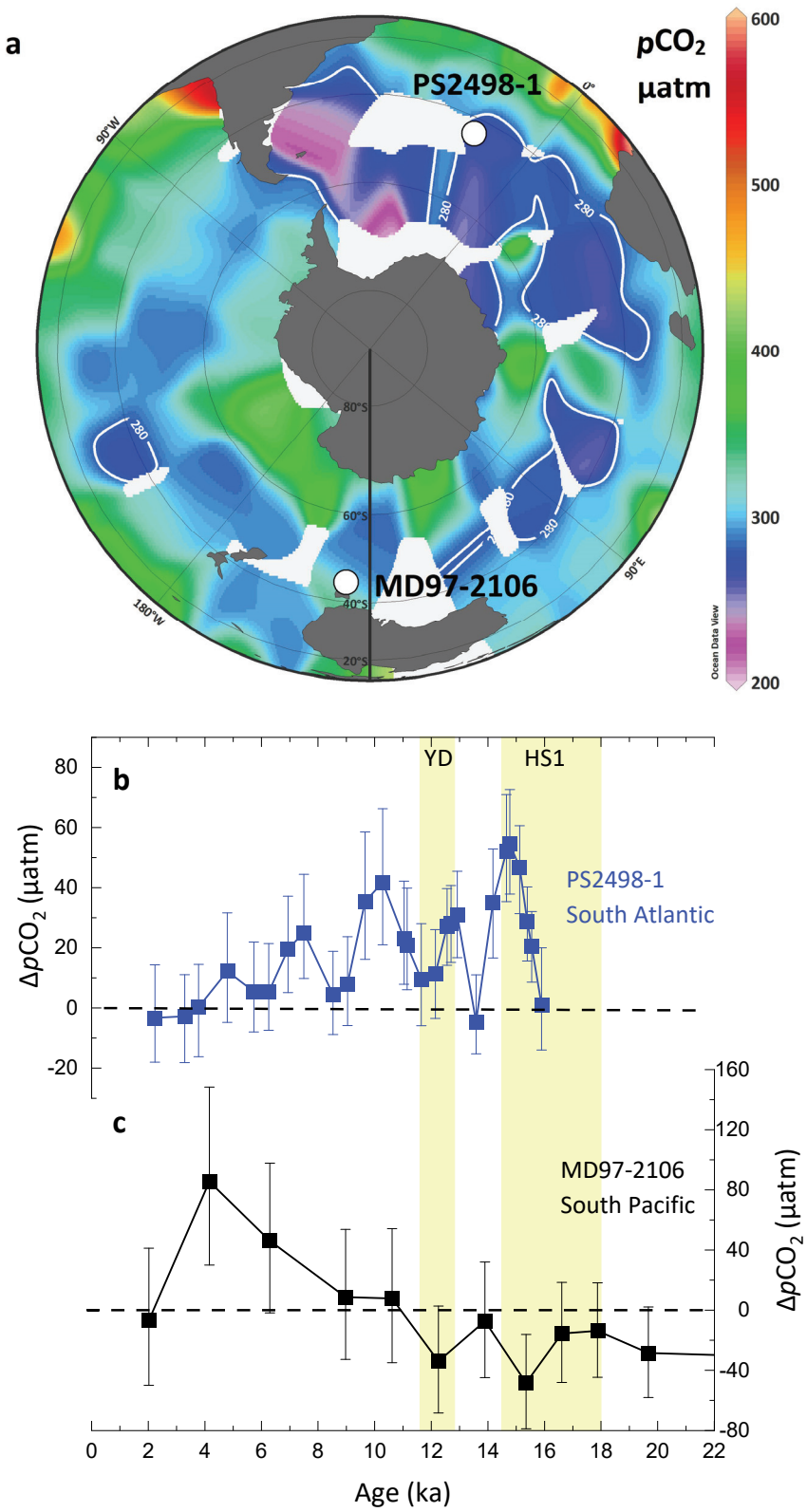
a
pCO2
µatm
PS2498-1
MD97-2106
280
90°W
0°
90°E
180°W
80°S
60°S
40°S
20°S
600
500
400
300
200
Ocean Data View
b
YD
HS1
PS2498-1
South Atlantic
ΔpCO2 (µatm)
c
MD97-2106
South Pacific
ΔpCO2 (µatm)
Age (ka)

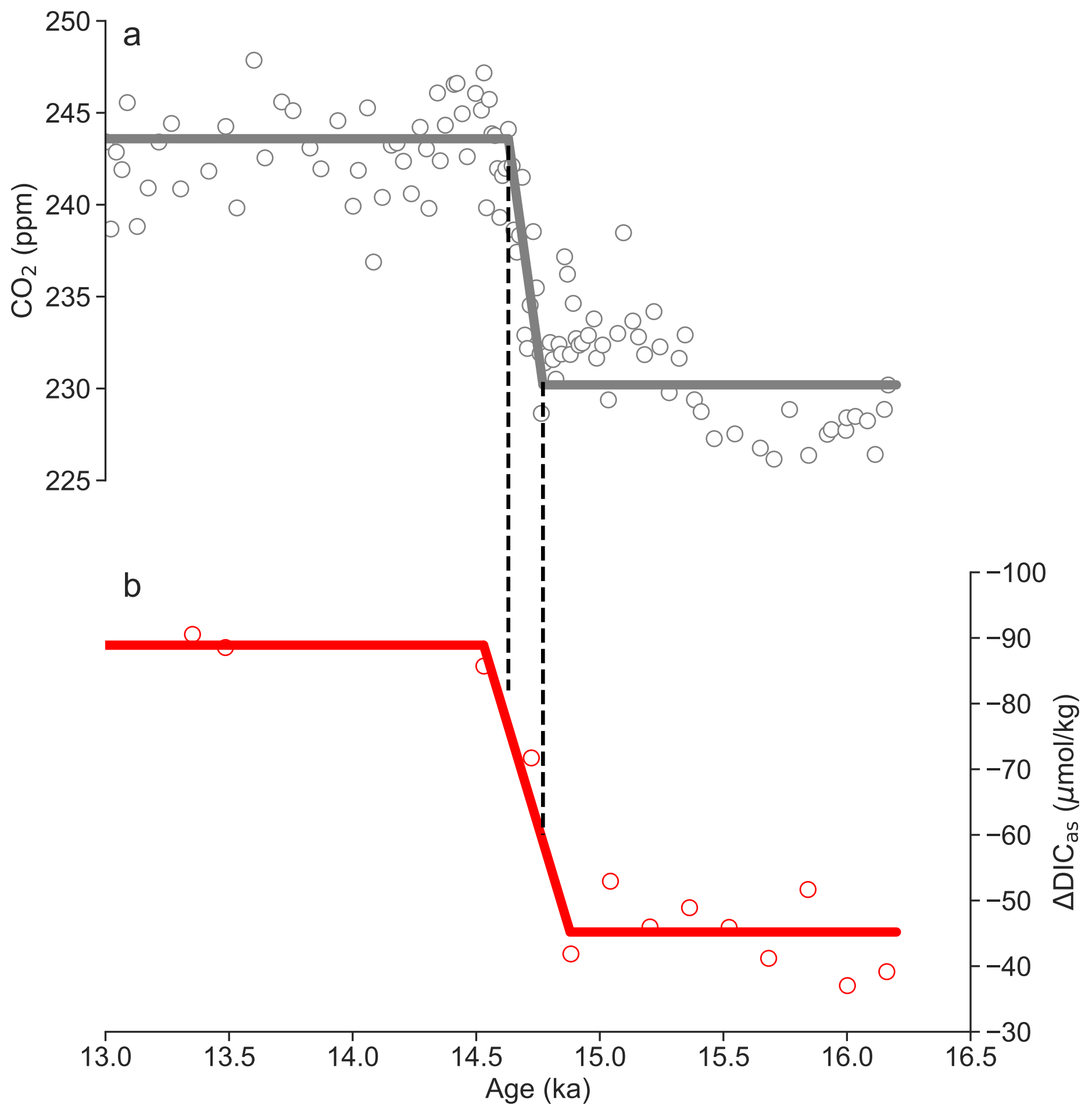
a
b
250
245
240
235
230
225
CO_2 (ppm)
−100
−90
−80
−70
−60
−50
−40
−30
ΔDIC_{as} (μmol/kg)
13.0
13.5
14.0
14.5
15.0
15.5
16.0
16.5
Age (ka)

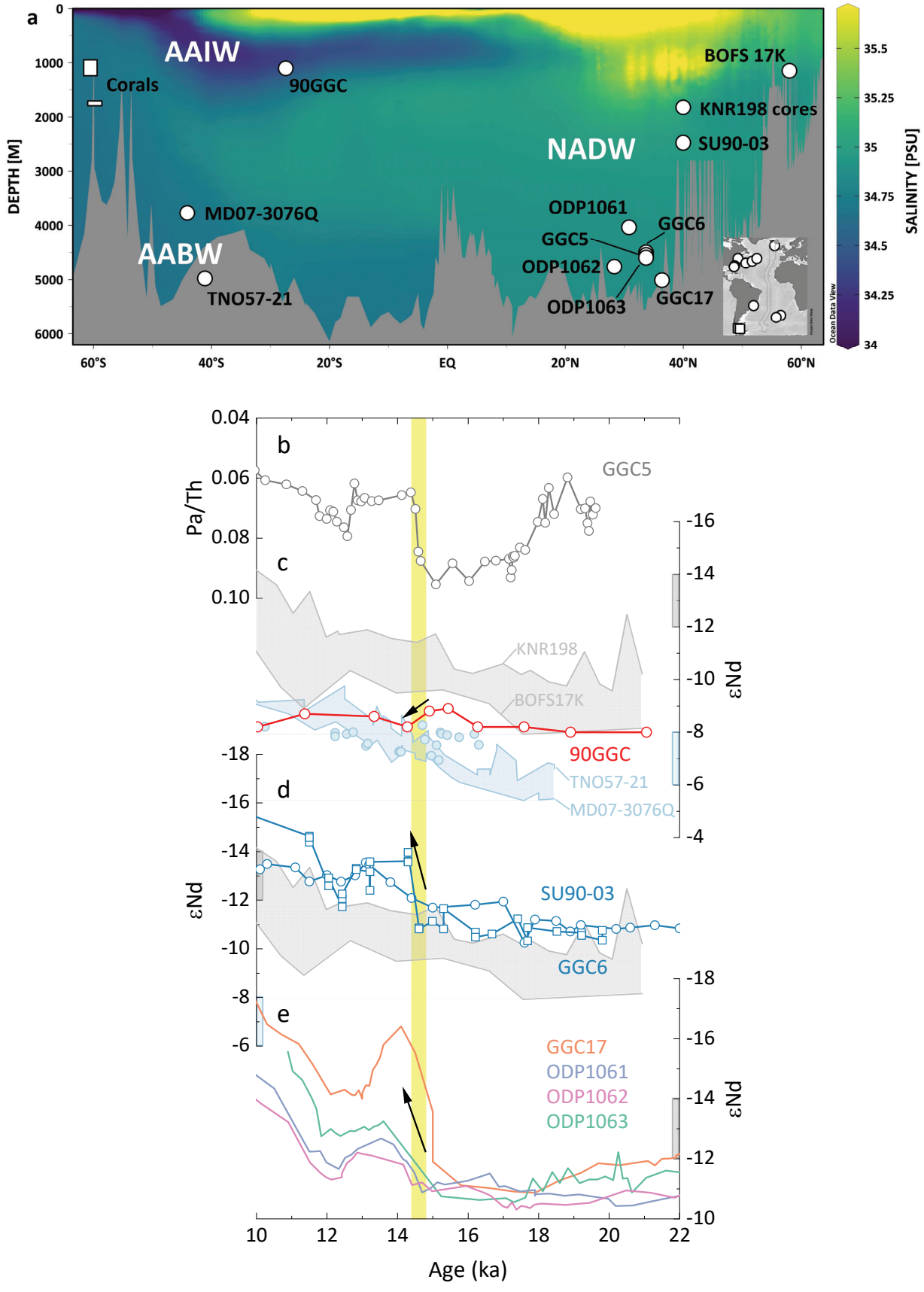
a
AAIW
NADW
AABW
Corals
90GGC
BOFS 17K
KNR198 cores
SU90-03
MD07-3076Q
ODP1061
GGC6
GGC5
ODP1062
GGC17
ODP1063
TNO57-21
DEPTH [M]
SALINITY [PSU]
60°S
40°S
20°S
EQ
20°N
40°N
60°N
b
GGC5
c
KNR198
BOFS17K
90GGC
TNO57-21
MD07-3076Q
d
SU90-03
GGC6
e
GGC17
ODP1061
ODP1062
ODP1063
Pa/Th
εNd
Age (ka)

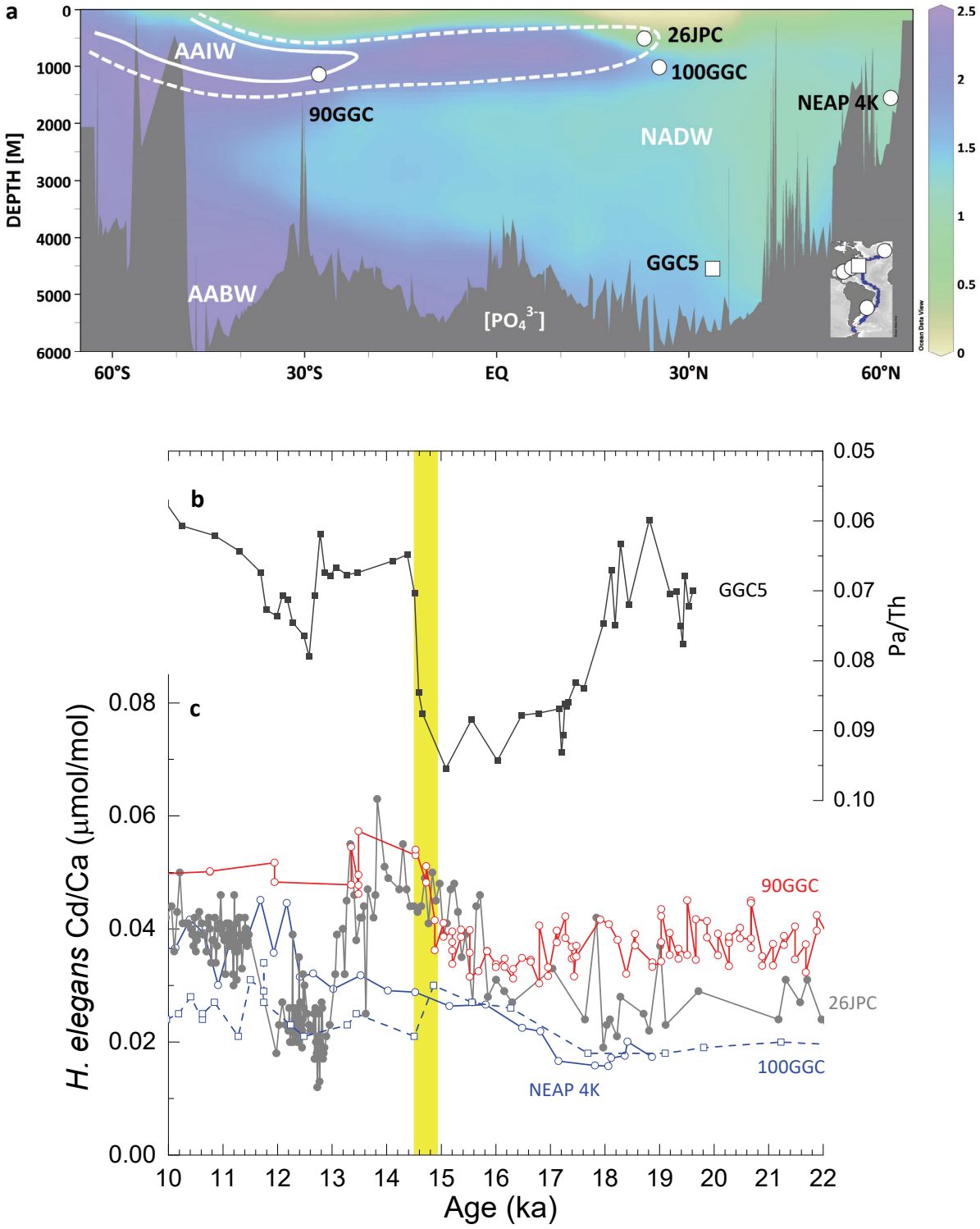
a
DEPTH [M]
0
1000
2000
3000
4000
5000
6000
60°S
30°S
EQ
30°N
60°N
AAIW
AABW
NADW
26JPC
100GGC
90GGC
NEAP 4K
GGC5
[PO4 3-]
2.5
2
1.5
1
0.5
0
b
GGC5
Pa/Th
0.05
0.06
0.07
0.08
0.09
0.10
c
H. elegans Cd/Ca (µmol/mol)
0.00
0.02
0.04
0.06
0.08
90GGC
26JPC
100GGC
NEAP 4K
10
11
12
13
14
15
16
17
18
19
20
21
22
Age (ka)

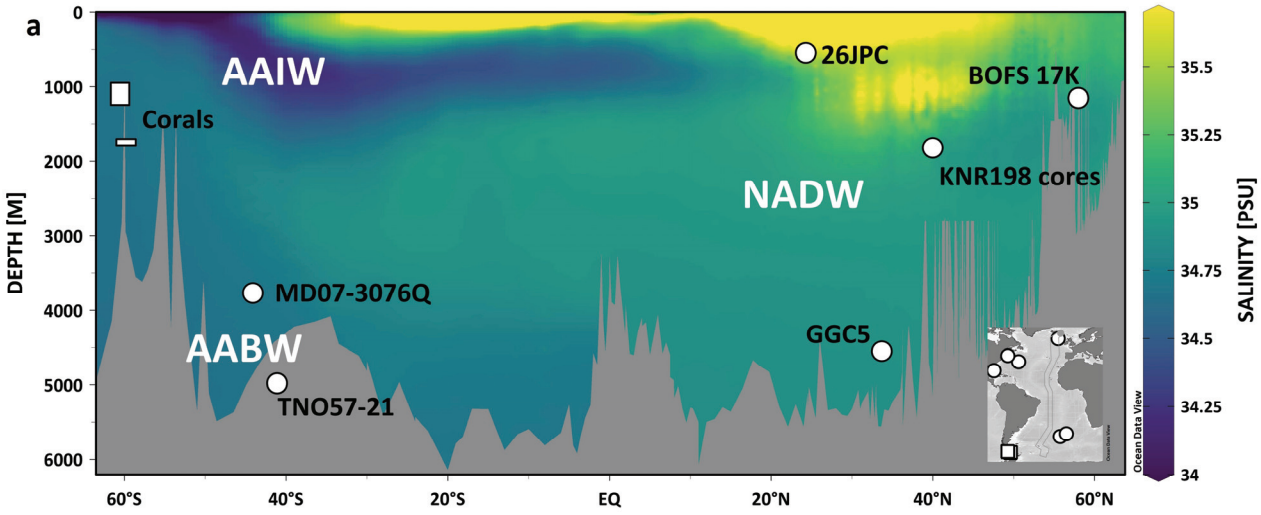
a
AAIW
26JPC
BOFS 17K
Corals
KNR198 cores
NADW
MD07-3076Q
AABW
GGC5
TNO57-21
DEPTH [M]
SALINITY [PSU]
0
1000
2000
3000
4000
5000
6000
35.5
35.25
35
34.75
34.5
34.25
34
60°S
40°S
20°S
EQ
20°N
40°N
60°N
Ocean Data View

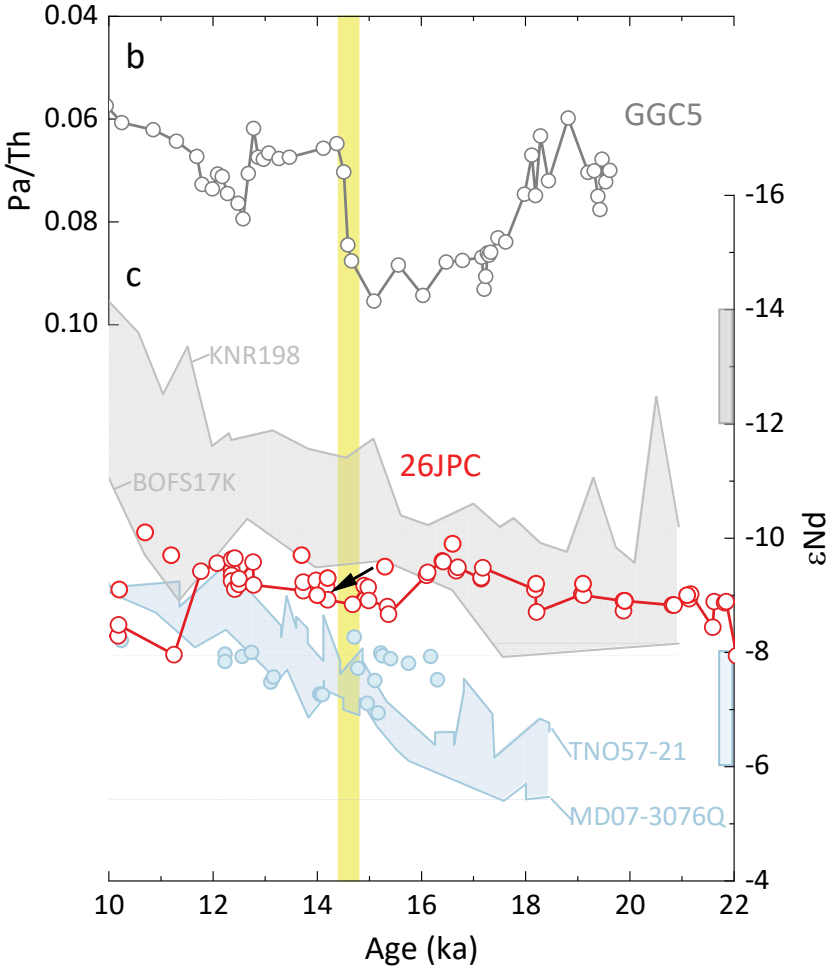
b
GGC5
Pa/Th
0.04
0.06
0.08
0.10
c
KNR198
BOFS17K
26JPC
TNO57-21
MD07-3076Q
εNd
-16
-14
-12
-10
-8
-6
-4
10
12
14
16
18
20
22
Age (ka)

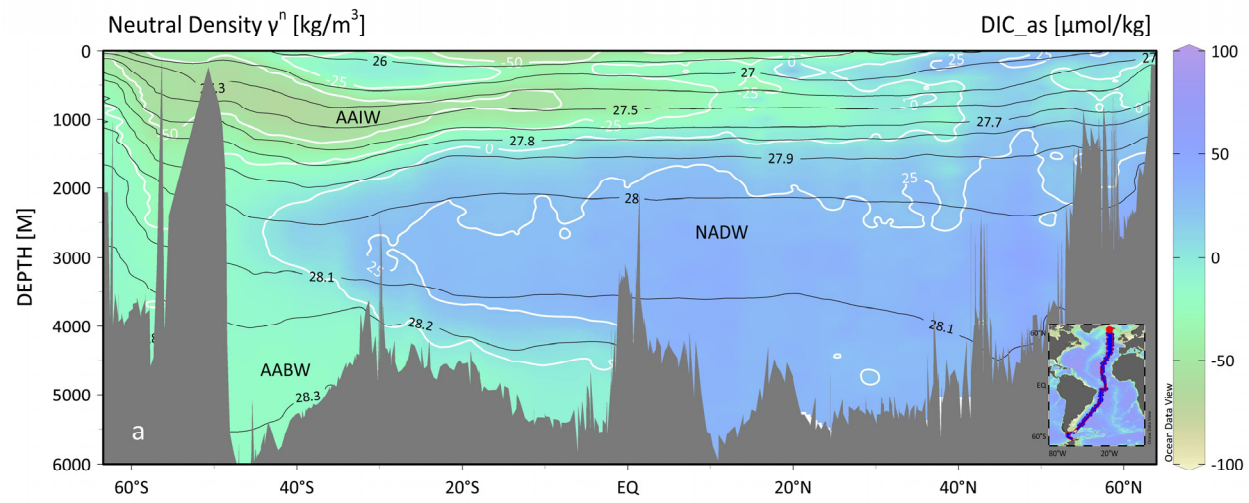
Neutral Density γ^n [kg/m^3]
DIC_as [µmol/kg]
DEPTH [M]
AAIW
NADW
AABW
a
60°S
40°S
20°S
EQ
20°N
40°N
60°N
Ocean Data View

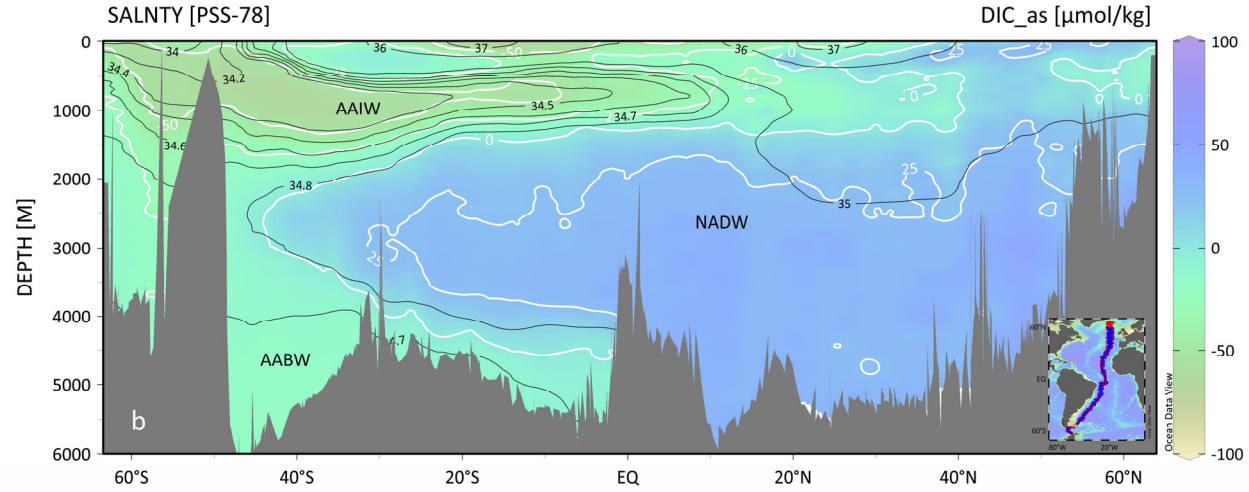
SALNTY [PSS-78]
DIC_as [µmol/kg]
DEPTH [M]
AAIW
NADW
AABW
b
60°S
40°S
20°S
EQ
20°N
40°N
60°N
Ocean Data View